Geophys. J. Int. (2004) **157,** 664–682 doi: 10.1111/j.1365-246X.2004.02217.x

Upper-mantle reflectors: modelling of seismic wavefield characteristics and tectonic implications

T. M. Hansen[1] and N. Balling[2]

[1]*Niels Bohr Institute for Astronomy, Physics and Geophysics, Department of Geophysics, Juliane Maries Vej* 30, 2100 *Copenhagen E, Denmark. E-mail: tmh@gfy.ku.dk*

[2]*Department of Earth Sciences, Geophysical Laboratory, University of Aarhus, Finlandsgade* 8, 8200 *Aarhus N, Denmark*

Accepted 2003 November 15. Received 2003 November 15; in original form 2003 January 6

SUMMARY

Deep seismic experiments on continental lithosphere generally reveal marked reflectivity from structures in the crust and a significant decrease in reflectivity from the upper mantle. However, reflected and refracted energy from mantle lithosphere are observed in both near-normal incidence and wide-angle data. The origin of the reflective structures is a matter of debate. Hypotheses include remnant subduction zones, shear zones, fluids and seismic anisotropy. Through analytical and numerical modelling studies, including full wavefield modelling, we investigate seismic characteristic signatures generated from a variety of geologically plausible models.

We have found that both upper-mantle shear zones of reduced velocity and density and remnant subduction slabs containing high-density eclogites may contain sufficient seismic impedance contrasts to normal mantle peridotites to generate near-normal incidence reflectivity. Wide-angle energy originates from subduction slabs containing either high- or low-velocity eclogites, whereas intermediate-velocity eclogites are unlikely to produce significant wide-angle phases. In general, energy of seismic phases originating from upper-mantle zones of anomalous seismic velocities and densities is significantly increased if homogeneous zones are replaced by zones of inhomogeneous petrophysical properties resulting from constructive interference. Maximum wavefield anomalies are generated from sub Moho dipping slabs of incomplete transformation of low-velocity/low-density crustal material to high-velocity/high-density eclogites. Localized shear zones generated in mantle peridotite generally do not produce significant wide-angle energy. Only if highly inhomogeneous structures containing material of marked (*ca* 10 per cent) velocity and density reduction are present, may shear zones be observed in wide-angle data.

Analyses of two specific deep-seismic data sets (MONA LISA data) from the North Sea and (BABEL data) from the Baltic Sea, show good agreement between observations and modelling results for dipping remnant subduction slabs containing small-scale inhomogeneities associated with incomplete transformation.

Our modelling results improve our possibilities of distinguishing between two often contrasting tectonic interpretations for dipping upper-mantle seismic reflectors, the remnant subduction and shear zone models.

Key words: eclogite, reflection seismology, refraction seismology, remnant subduction, shear zones, upper mantle.

1 INTRODUCTION

Seismic velocity structure in the crust and uppermost mantle can be resolved by seismic refraction and wide-angle reflection experiments and details of reflectivity structure by the near-normal incidence seismic reflection technique. For many continental areas, deep seismic reflection sections show marked reflectivity from the crust and an almost transparent uppermost mantle. The first significant reflective structures from the mantle lithosphere, including the spectacular Flannan and W-reflectors, were observed by the BIRPS group on several deep seismic lines northwest of Scotland (e.g. Smythe *et al.* 1982; Flack *et al.* 1990). In recent years, several seismic experiments have demonstrated the existence of seismic reflectors in the mantle lithosphere (Lie *et al.* 1990; BABEL Working

Group 1990; Posgay *et al.* 1990; Calvert *et al.* 1995; Alsdorf *et al.* 1996; Knapp *et al.* 1996; MONA LISA Working Group 1997a; Cook *et al.* 1998, 1999; DEKORP-BASIN Research Group 1999; ANCORP Working Group 1999; Balling 2000). Consequently, the uppermost mantle locally contains petrophysical contrasts sufficiently large to be resolved as seismic reflectors. The mantle lithosphere has become a new frontier for very deep seismic profiling (Steer *et al.* 1998). As a consequence, primarily, of the results of deep seismic experiments, the existence of significant structures in the uppermost mantle is no longer a matter of debate, however, there is no general agreement concerning their origin.

In this paper we investigate which seismic signatures (wide-angle as well as normal-incidence) can be expected from geologically plausible models, and which petrophysical parameters and types of rocks are needed to produce seismic energy similar to that observed in deep seismic experiments. In our analysis, we use analytical results based upon Zoeppritz equations and numerical full waveform modelling.

2 GEOLOGICAL MODELS FOR UPPER-MANTLE REFLECTIVITY

Warner & McGeary (1987) point out that the strong reflective energy observed from the uppermost mantle in BIRPS' deep seismic reflection profiles northwest of Scotland, with an apparent reflection coefficient of approximately 0.1, can be explained neither by layering nor by anisotropy of olivine and pyroxene, the typical upper-mantle minerals. Some other material must be present. Several geological models have been proposed to explain such upper-mantle reflectivity. The most widely addressed models are relict subduction zones (BABEL Working Group 1990; Calvert *et al.* 1995; Warner *et al.* 1996; Cook *et al.* 1999; Balling 2000) and mantle shear zones (e.g. Klemperer & White 1989; Reston 1990; Abramovitz *et al.* 1998; Nielsen *et al.* 2000). In conjunction with these two models, seismic anisotropy and fluids may additionally generate reflections. Dipping reflectivity is observed in active subduction zones and may, at least in part, be related to fluids (Clowes *et al.* 1987; Calvert & Clowes 1990; ANCORP Working Group 1999).

2.1 Relict subduction and collision

When oceanic crust is subducted to a depth greater than *ca* 40 km, it enters the stability field of eclogite. Eclogite facies conditions exist at temperatures $>500^\circ$C and pressures >1.2 GPa. Full transformation from basalt/gabbro to eclogite may not readily occur. In general, some overstepping of equilibrium conditions is needed. Both laboratory experiments and field observations show that the presence of water significantly stimulates transformation (see Hacker 1996 for a review).

The mantle reflectors observed north of Scotland have been subject to comprehensive studies. Recent integrated analysis of both near-normal incidence and wide-angle seismic data from the Flannan and the W-reflector show that both reflectors are of positive polarity. Modelling of wide-angle data from the W-reflector gives a layer 3–10 km thick with a P-wave velocity of 8.5 ± 0.1 km s^{-1} and a density of 3500 ± 50 kg m^{-3} embedded in upper mantle of normal physical properties (P-wave velocity of 8.2 km s^{-1} and density of 3350 kg m^{-3}). These observations clearly suggest that the Flannan and W-reflectors represent reflection events from the tops of slabs of eclogite and the above authors unequivocal favour the subduction hypothesis for these mantle reflectors. Oceanic crust, or fragments of oceanic crust, have been subducted and metamorphosed to eclogite facies.

Interpretation in terms of relics of ancient subduction and collision zones has been advocated for dipping upper-mantle reflectors observed in BABEL data from the Baltic shield (BABEL Working Group 1990; Balling 2000) and MONA LISA data from the North sea (MONA LISA Working Group 1997b; Balling 2000).

Among the most spectacular upper-mantle reflectors seen so far are those recently discovered by LITHOPROBE in the western Canadian shield (Cook *et al.* 1998, 1999). Here the SNORCLE transect shows clear correlated mantle reflectors along *ca* 500 km profiles, where reflections are observed from the crust–mantle boundary to 23–26 s twt (two way travel time) (80–95 km depth). Reflectors are interpreted to originate mainly from 1.9–1.8 Gyr old frozen subduction structures (Cook *et al.* 1999).

Characteristic structural features seem to apply to many of these upper-mantle reflectors interpreted to represent ancient subduction zones. The crust–mantle boundary may show marked topography including thickened crust and Moho offsets where reflectors leave the crust–mantle boundary and dip into the upper mantle generally at rather low angles between 15° and 30° (*cf.* BABEL Working Group 1990; Calvert *et al.* 1995; Cook *et al.* 1999; Balling 2000).

2.2 Shear zones

It is generally accepted that seismic reflectivity may be generated by crustal faults and shear zones (Meissner 1996) that can be formed both in compressional and extensional regimes. Combined laboratory petrophysical measurements, field studies and synthetic reflection modelling and comparison with crustal seismic reflection sections (e.g. Jones & Nur 1982, 1984; Fountain *et al.* 1984; Christensen & Szymanski 1988; Wang *et al.* 1989; Shaocheng *et al.* 1997) have shown that contrasting seismic impedance associated with shear zones, mainly resulting from mylonites, is sufficient to cause prominent reflectivity similar to observations. For example, Christensen & Szymanski (1988) found that seismic reflections originate within the Brevard fault zone (a 0.5 to 3 km wide belt of mylonitic and low-grade metamorphic rocks extending for more than l700 km from central Alabama into Virginia, USA) from complex interaction of compositional variations and seismic anisotropy resulting from ductile strain.

Much less observational information is available for mantle shear zones. However, field evidence from Alpine (Vissers *et al.* 1991, 1995) as well as north Pyrenean (Vissers *et al.* 1997) exposed upper-mantle peridotites demonstrate the existence of localized mylonite shear zones that developed under uppermost mantle temperature and pressure conditions. Microstructures and mineralogic analyses of these mylonite zones are interpreted to reflect progressive, reaction-related grain-size reduction and localization of deformation during lithosphere extension. Both hydrated (Alps) and dry (Pyrenees) reaction environments are observed.

Using numerical geodynamic modelling, Frederiksen & Braun (2001) show that extension of the lithosphere leads to strain localization if mantle rocks show a strain softening behaviour. Strain localizations include approximately 45° dipping almost linear shear bands that cut through the mantle lithosphere. These results, combined with seismic evidence of dipping upper-mantle reflectors observed in tectonic environments where basin forming lithospheric extensional events have occurred, such as in the North Sea (Klemperer & White 1989; Reston 1990; Nielsen *et al.* 2000; Frederiksen *et al.* 2001), support the assumption that localized mantle shear zones exist and may be observed in seismic reflection sections.

Meissner & Krawczyk (1999), Meissner *et al.* (2002) and Krawczyk *et al.* (2002) argue that a number of north/northeast dipping mantle reflectors observed in the Baltic Sea along the Trans-European Suture Zone (TESZ) may represent compressive faults or shears not necessarily related to previous subduction of oceanic crust.

Upper-mantle faults and shear zones generated in compressional tectonic regimes may be associated with areas of thickened crust, Moho topography and Moho offsets similar to fossil subduction features discussed above, whereas extensional shear is more likely to be observed beneath thinned crust with only minor Moho topography, as seen in several places in the North Sea. Of course, quite complex situations may occur if compressional shear structures are later reactivated in extensional regimes or if extensional shears are reactivated in compressional regimes.

2.3 Anisotropy

Olivine, which is expected to constitute about two thirds of upper-mantle minerals, is highly anisotropic. When oriented by an appropriate stress system, large parts of the upper mantle may develop anisotropy. Other mantle minerals are much less anisotropic (Anderson 1989). In assemblages of mantle minerals, velocity anisotropy larger than 5 per cent is uncommon. Eclogite shows less than 3 per cent anisotropy. Dunite, consisting mainly of olivine, has the potential of high *P*-wave velocity anisotropy of approximately 8.1 ± 3.9 per cent, (table 5 in Christensen & Mooney 1995). The detection of up to 7–8 per cent azimuthal seismic velocity anisotropy beneath both continents and oceans (Anderson 1989) indicates that the uppermost mantle may contain oriented olivine. Warner & McGeary (1987) found that anisotropy in upper-mantle peridotite will lead to reflection coefficients of less than 0.04, which is too little to account for the most significant seismic reflectors. However, as for crustal shears, localized deformation in the upper mantle may result in some anisotropy of seismic velocity and contribute to the generation of reflectivity, partly as a result of inhomogeneity of structures.

2.4 Fluids

The presence of even very small amounts of water or melt will have strong effects on seismic waves. As a result of fluids having zero shear modulus, a large contrast to solid rocks will exist and may well cause significant reflectivity. In young subduction regimes, fluids are likely to be present along the upper part of a subduction slab and may generate reflectivity from the top of the subducting slab (ANCORP Working Group 1999). For older tectonic regimes, it is likely that most fluids have migrated away or have been absorbed into mineral reactions. In general, in young tectonic regimes it is reasonable to assume that fluids may be present and influence seismic properties.

3 SEISMIC CHARACTERISTICS OF UPPER-MANTLE STRUCTURES

In this section we will define typical upper-mantle material and for two specific cases, a subduction model and a shear zone model, investigate the effects on reflectivity of likely physical deviations from typical average mantle properties. Amplitude versus offset (AVO) patterns, implied by variations in elastic parameters across a plane interface between two elastic solids is investigated using the fundamental Zoeppritz equations. Reflected and scattered wavefields from more complex structures including zones of random-parameter distributions are studied using numerical finite difference techniques.

3.1 Petrophysical models

Based on Christensen & Mooney (1995), amongst others, we use a peridotite reference model for the uppermost mantle with *P*-wave velocity (Vp) of 8.1 km s^{-1} and density (ρ) of 3350 kg m^{-3}. *S*-wave velocity is calculated as $V_s = V_p/1.64$, following Sobolev & Babeyko (1994). Alternative use of a ratio between 1.7 and 1.75 observed for many mantle peridotites (e.g. Anderson 1989) will not change out modelling results significantly.

3.1.1 Relict subduction zones

Unlike active subduction zones, relict subduction zones beneath old continental crust, are unlikely to include free fluids in significant amounts. The most significant petrophysical contrasts are likely to be associated with the transformations to eclogite of former oceanic basaltic crust (*cf.* Warner *et al.* 1996; Morgan *et al.* 2000; Price & Morgan 2000). Density increases significantly and may reach values above that of normal upper mantle, depending on the degree of transformation from basalt/gabbro to eclogite. Anderson (1989, table 3–8) lists measured densities and seismic velocities for different eclogites. Density is generally large, 3470–3610 kg m^{-3}. Christensen & Mooney (1995) report average density for eclogite as 3480 ± 70 kg m^{-3}. Eclogite is consistently found to have a density larger than that of normal upper-mantle peridotite. *P*-wave velocity of eclogites shows a large range. Christensen & Mooney (1995) report average eclogite Vp of around 7.9 km s^{-1}. Anderson (1989) lists velocities ranging from 8.2 to 8.6 km s^{-1} and Rudnick & Fountain (1995) report eclogite velocities between 7.7 km s^{-1} and 8.6 km s^{-1}. The highest velocities are found for garnet-rich eclogites. Measurements of *S*-wave velocity are less common, however, in general the Vp/Vs ratio is larger for eclogites than for other types of upper-mantle rocks. Anderson (1989, tables 3–8) lists Vp/Vs ratios as between 1.73 and 1.85.

Thus, in general, it is agreed that the density of a slab of eclogite in the mantle is larger than its surroundings. We use $\rho = 3550$ kg m^{-3}. The *P*-wave velocity in the eclogites shows a wide range. In the following tests we use 7.4 km s^{-1} $< Vp <$ 8.6 km s^{-1} and $Vs = Vp/1.8$.

3.1.2 Shear zones

As discussed above, faults and shear zones in the upper mantle are likely to result in complex structures and petrophysical properties. Crustal shear zones seem, generally, to represent zones of reduced seismic impedance (Meissner 1996 and references therein). Grain size reduction and mineral reaction including formation of amphiboles, plagioclase and chlorite as observed in exposed upper-mantle peridotites (Vissers *et al.* 1995, 1997) also point towards a reduction in *P*-wave velocity and density for upper-mantle rocks. Observed thicknesses of significantly changed mineralogy and physical properties vary significantly from very narrow zones to kilometre scale. Based upon observations from north Pyrrenean peridotites, Vissers *et al.* (1997) applied zones of up to 5 km thickness in their rheological models. As a result of a lack of detailed experimental information on the petrophysical properties of upper-mantle shear zones, we

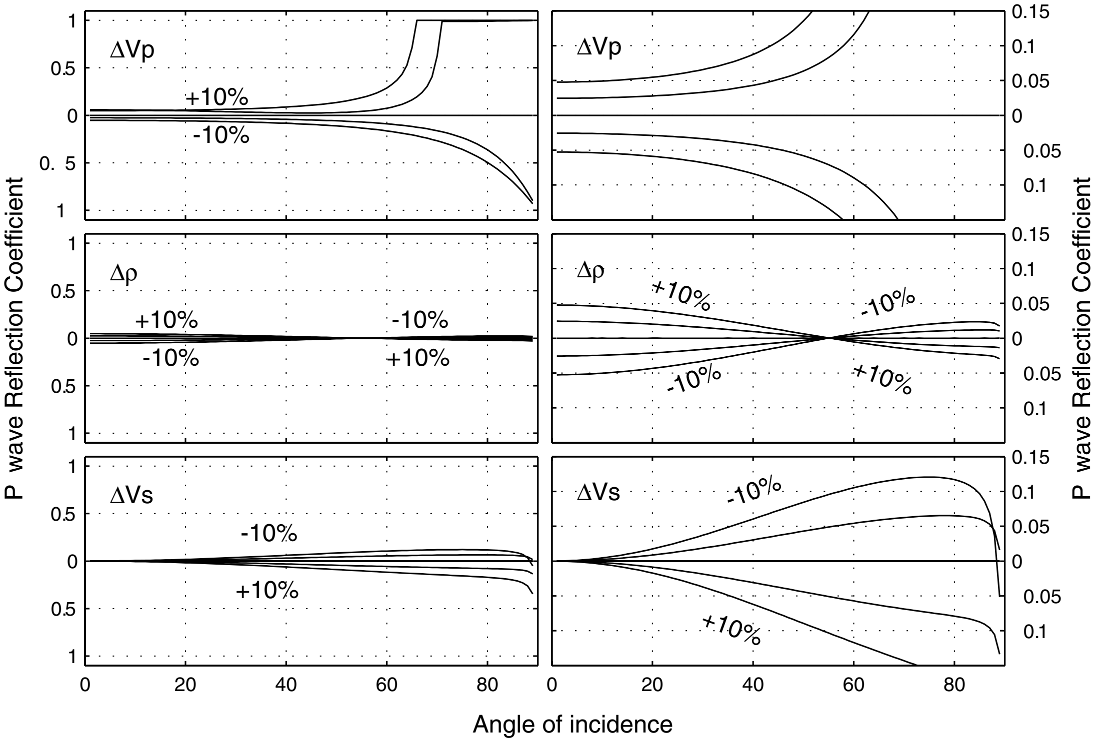

Figure 1. Effect on the reflection coefficient for varying Vp (top), ρ (middle) and Vs (bottom) by ±10 per cent across a boundary between two elastic solids. Elastic properties above the boundary are: $Vp_1 = 8.1$ km s^{-1}, $Vs_1 = (1/1.64) \times Vp_1 = 4.9$ km s^{-1} and $\rho_1 = 3350$ kg m^{-3}. Below the boundary Vp, ρ and Vs are changed by: −10, −5, 0, 5 and 10 per cent. Plots to the right are similar to plots to the left except a narrower reflection coefficient range is plotted. For complex coefficients, the absolute value is plotted.

will analyse a variety of models that include separate variations in *P*-wave velocity, *S*-wave velocity and density.

3.2 Reflectivity from a plane interface

Zoeppritz' equations describe the relation between the amplitudes of incoming *P* and *S* waves and the reflected and transmitted waves they generate across a plane interface between two elastic solid homogeneous half-spaces, (e.g. Achenbach 1973). These relations are used to investigate basic seismic characteristics resulting from changes in the elastic parameters for anomalous upper-mantle material embedded in typical mantle material.

3.2.1 Reflectivity characterization of contrasts in density and velocity

Fig. 1 shows the variation of amplitude with offset of a reflected *P*-wave when one elastic parameter increases or decreases across the interface by up to 10 per cent while the other two are held constant. Critically reflected energy naturally appears when the *P*-wave velocity increases. The higher the *P*-wave velocity, the shorter the offset to the point of critical reflected energy. For offsets beyond critical distance, the reflection coefficient will stay high, however, a gradual phase change deforms the wavelet from a positive to a negative shape (not shown).

Variation in density results in a less dramatic variation in reflectivity. At near-normal incidence, the effect is the same as for perturbations in *P*-wave velocity. At an incidence of approximately 55° corresponding to an offset/depth ratio of approximately 3.5, the *P*-wave reflectivity has a zero crossing for all density contrasts. At longer offsets the reflectivity remains moderate. Thus, variation in density causes reflected energy mainly at small offsets.

Changes in *S*-wave velocity do not lead to reflected *P*-wave energy at small offsets, however, at larger offsets (incidence angles of 65°–70°) the reflection coefficient becomes almost constant as a function of offset. The level of the reflection amplitude is comparable to that related to changes in the *P*-wave, except around and above the critical angle.

3.2.2 Reflectivity from eclogite–peridotite interfaces

Fig. 2 shows the amplitude versus angle pattern to be expected for alternative, likely eclogite, slabs embedded in normal mantle peridotite. We note that a low-velocity eclogite is almost transparent at near-normal incidence, whereas it will show a moderate negative reflectivity at wide-incidence angles. A high-velocity eclogite will reflect strongly at near-normal incidence and even more so around and beyond the critical angle. The bottom of a low-velocity eclogite slab will reflect strongly at very wide angles, however, the incidence remains subcritical because of the steepening refraction at the top of the slab.

Thus, observation of strong wide-angle reflections would favour high-velocity eclogites over low-velocity eclogites. However, the lack of critical reflection from the bottom of a low-velocity eclogite depends on the slab geometry. If structures are more complex this limitation may not apply, as will be studied more generally in the following sections.

Reflection from layers with a thickness of less than a quarter of a wavelength ($\lambda/4$) are subject to tuning effects, which is not modelled by Zoeppritz' equations. For the data we have worked

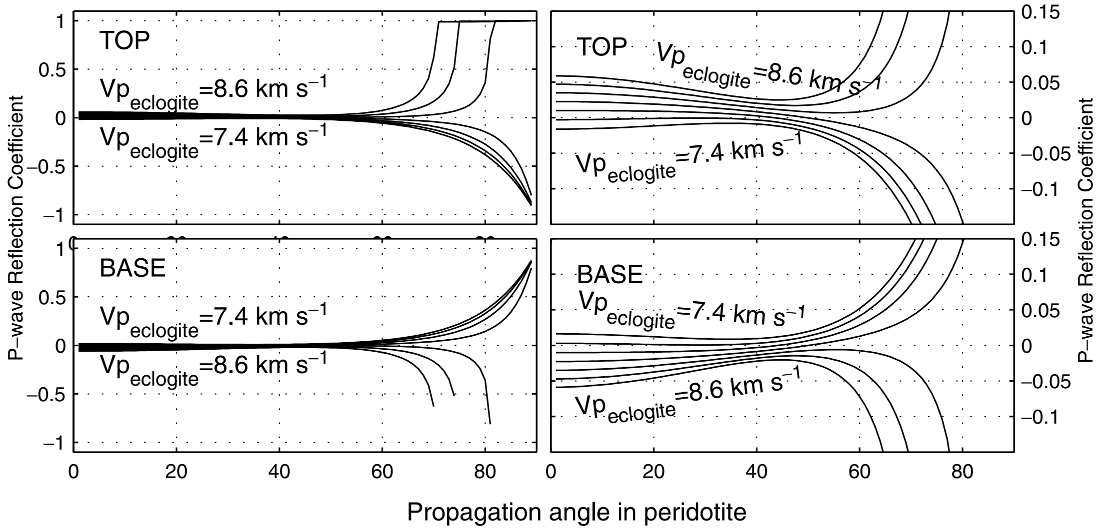

Figure 2. *P*-wave reflection coefficient from the top and base of a layer of eclogite embedded in normal mantle peridotite with $Vp = 8.1$ km s^{-1}, $Vs = Vp/1.64 = 4.9$ km s^{-1} and $\rho = 3350$ kg m^{-3}. The material in the layer represents various types of eclogite with $Vp = 7.4$, 7.6, 7.8, 8.0, 8.2, 8.4, 8.6 km s^{-1} and $Vs = Vp/1.8$. All models have $\rho = 3550$ kg m^{-3}. Plots to the right are similar to plots to the left except a narrower reflection coefficient range is plotted.

with in this paper, an 8 Hz peak frequency is typical, resulting in a dominant wavelength of approximately 1 km in the upper mantle (for $Vp = 8$ km s^{-1}). Such tuning effects can both increase and decrease the amplitude and change the waveform. A very thin layer ($<\lambda/8$) embedded in the upper mantle will typically show a decrease in amplitude. The thinner the layer, the closer to zero will be the reflectivity. An increase in amplitude for a layer thickness of $\lambda/4$ of approximately 40 per cent is possible (see e.g. fig. 6.42b in Sheriff & Geldart 1995). In this paper, we do not investigate models with such thin layers, however, we acknowledge that for some special cases tuning effects from thin layers in the upper mantle will cause an increase in amplitude.

3.3 Reflectivity from a stochastic zone

The transformation into eclogite known from exposures often has an incomplete and erratic character (Austrheim *et al.* 1997). Therefore, we regard stochastic, partly fractal structures (Turcotte 1997) as possible models for mantle eclogites. Stochastic elastic models give rise to complex reflected/scattered wavefields that cannot be described using ray theory alone (Williamson & Worthington 1993). Tittgemeyer *et al.* (2000) show that a slightly complex region below the Moho can generate a *Pn* phase even when the velocity gradient below the Moho is negative. Within ray theory, *Pn* exists only with a positive gradient. Different types of stochastic or random media produce different reflectivity patterns, which give some qualitative information about the elastic properties of the region from which they are generated (Hurich 1996; Nielsen *et al.* 2003).

In the following sections, a series of randomly-distributed velocity fields will be used. They are created using a bimodal von Karman correlation function with horizontal and vertical correlation lengths $(a_x, A_z) = (1$ km, 0.2 km) and a Hurst number of $\nu = 0.6$. These stochastic properties are inspired by those observed (e.g. Levander *et al.* 1994). All finite difference modelling has been performed using main phase modelling, an efficient fourth-order space, second-order time finite difference implementation of the elastic wave equation (Hansen & Jacobsen 2002). The code is available from http://mpm.sourceforge.net/ A model of 600 km × 180 km sampled at 65 m wide grid cells using a Ricker wavelet with a peak frequency of 5 Hz was used to model the results in the coming section.

3.3.1 A slab with random distribution

Modelling results shown in Figs 3 and 4 may be viewed as a stochastic counterpart to the homogeneous slab computations displayed in Fig. 2. In a homogeneous model of typical upper-mantle material, a 7 km thick slab with a random-velocity distribution is introduced with its top at 40 km depth. The velocity distribution is defined using a bimodal von Karman correlation. It consists of 50 per cent reference material and 50 per cent material in which one of the parameters, *Vp*, *Vs* or ρ, is increased or decreased by 10 per cent.

Fig. 3 shows three compressional (*P*-waves only) wavefield snapshots for six models, each of which is defined by a decrease or increase of 10 per cent of *Vp*, *Vs* and ρ.

At near-normal incidence there is little to no difference between the wavefields induced by an increase or a decrease of any elastic parameter (Fig. 3b). For changes in *Vp*, the amplitude of the reflective wavefield shows almost the same amplitude for all angles of incidence. Changes in *Vs* give very little normal-incidence reflected energy, however, for incidence angles of approximately 45°, the reflected *P*-wave energy is of the same order as that produced by changes in *Vp*. Variation in density results in a normal-incidence reflected wavefield that resembles that of changes in Vp, while little to no energy is transmitted. This is in agreement with the Zoeppritz plots in Fig. 1.

When the wavefield has propagated out to a wider angle of incidence, (Fig. 3c), there is a clear difference between the *P*wavefield caused by a positive and negative perturbation of *Vp* in the slab. An increase in *P*-wave velocity of 10 per cent generates mostly one to two relatively strong phases following the reflected wave from the slab (Fig. 3c1), while a decrease in *P*-wave velocity of 10 per cent causes a chaotic wave pattern following the reflection from the slab and no distinct phases (Fig. 3c2). Positive and negative perturbations of *Vs* and ρ show much less variation. Perturbation of *Vs* causes *P*-wave energy perpendicular to the wave travel path (Figs 3c3 and

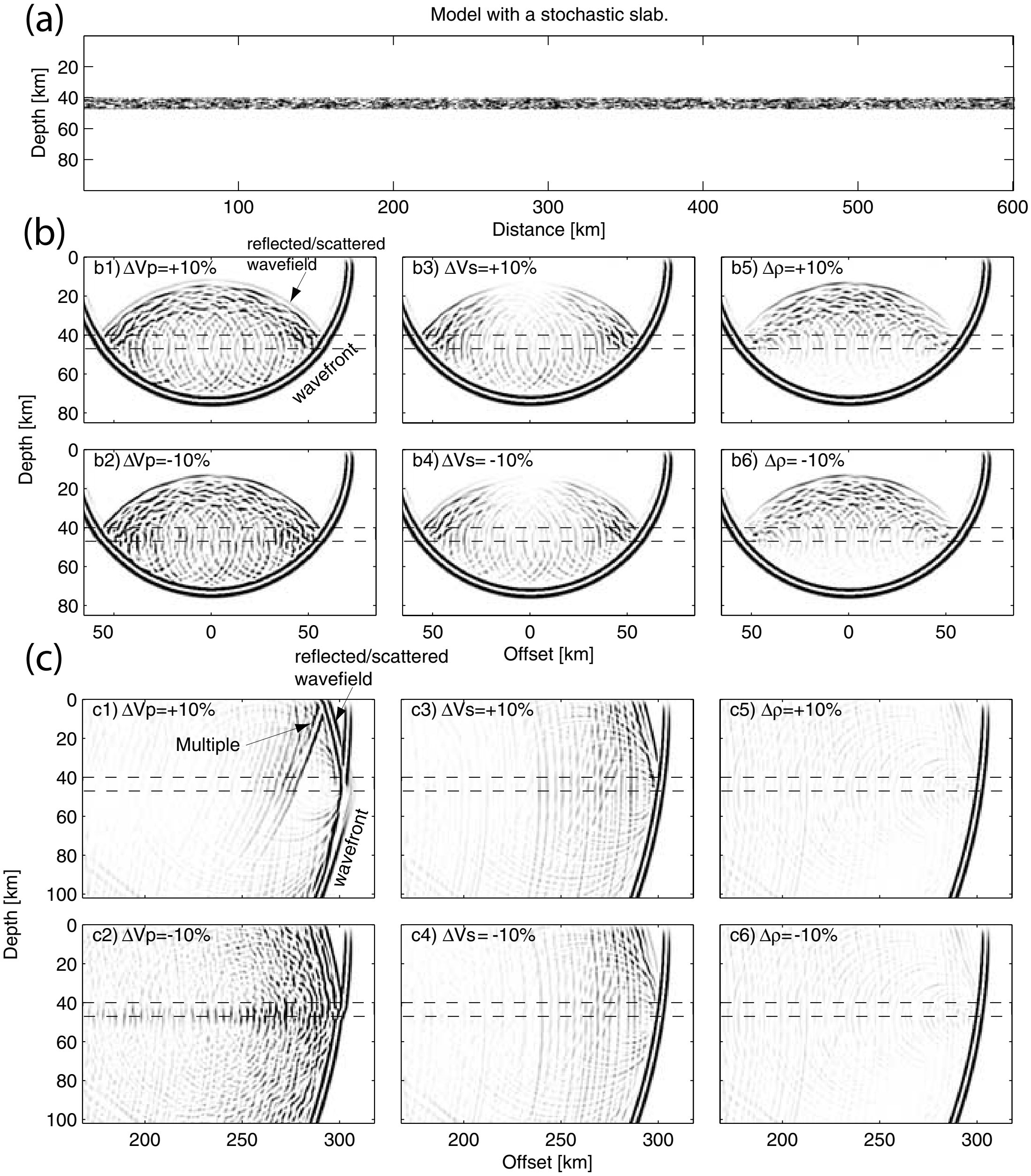

Figure 3. *P*-wavefield snapshots for perturbations of elastic parameters of a horizontal slab with a random velocity distribution. The reference model (a) is upper mantle ($Vp = 8.1$ km s^{-1}, $Vs = 4.9$ km s^{-1}, $\rho = 3350$ kg m^{-3}) with a 7 km thick slab at 40 km depth, with randomly distributed properties. The slab consists of 50 per cent reference material and 50 per cent material with a perturbation of one of the three investigated elastic parameters. The random model has a von Karman autocorrelation function, with horizontal and vertical correlation lengths $(a_x, a_z) = (1$ km, 0.2 km$)$ and a Hurst number of $\nu = 0.6$. Perturbations are by ± 10 per cent, as indicated. The wavefields shown have been propagated 9.6 s (b) and 38.2 s (c).

c4), while perturbation of ρ causes very little energy at wide-angles (Figs 3c5 and c6).

Reduced traveltime plots of the compressional wavefield modelled in Fig. 3 are shown in Fig. 4. It is evident that perturbation of *Vp* results in a clearly defined first arrival at all offsets. An increase of *Vp* causes little energy following the first arrival for longer offsets (Fig. 4a), while a decrease of *Vp* causes a double-phased first arrival, with relatively high-amplitude scattering following the first arrival (Fig. 4b). When *Vs* is perturbed, (Figs 4c and d) reflected *P*-wave energy is observed at shorter offsets, similar in amplitude to that of perturbation of *Vp*, while at longer offsets little reflected *P*-wave energy is observed. A slight tendency to a less focused wide-angle first arrival can be identified for an increase (Fig. 4c) rather than for a decrease (Fig. 4d) in *Vs*. The scattered wavefield following the first arrival for *Vs* perturbations is more coherent, however, it has an amplitude similar to that observed for a decrease in *Vp*. As expected, little to no energy is seen as a result of perturbation of ρ (Figs 4e and f). These results clearly demonstrate that small-scale velocity inhomogeneities strongly affect the wide-angle seismic wavefield.

3.4 Wide-angle characteristics from sub Moho structures

In addition to the fine structure of petrophysical parameter variation studied above, larger scale complexity of geological structures also

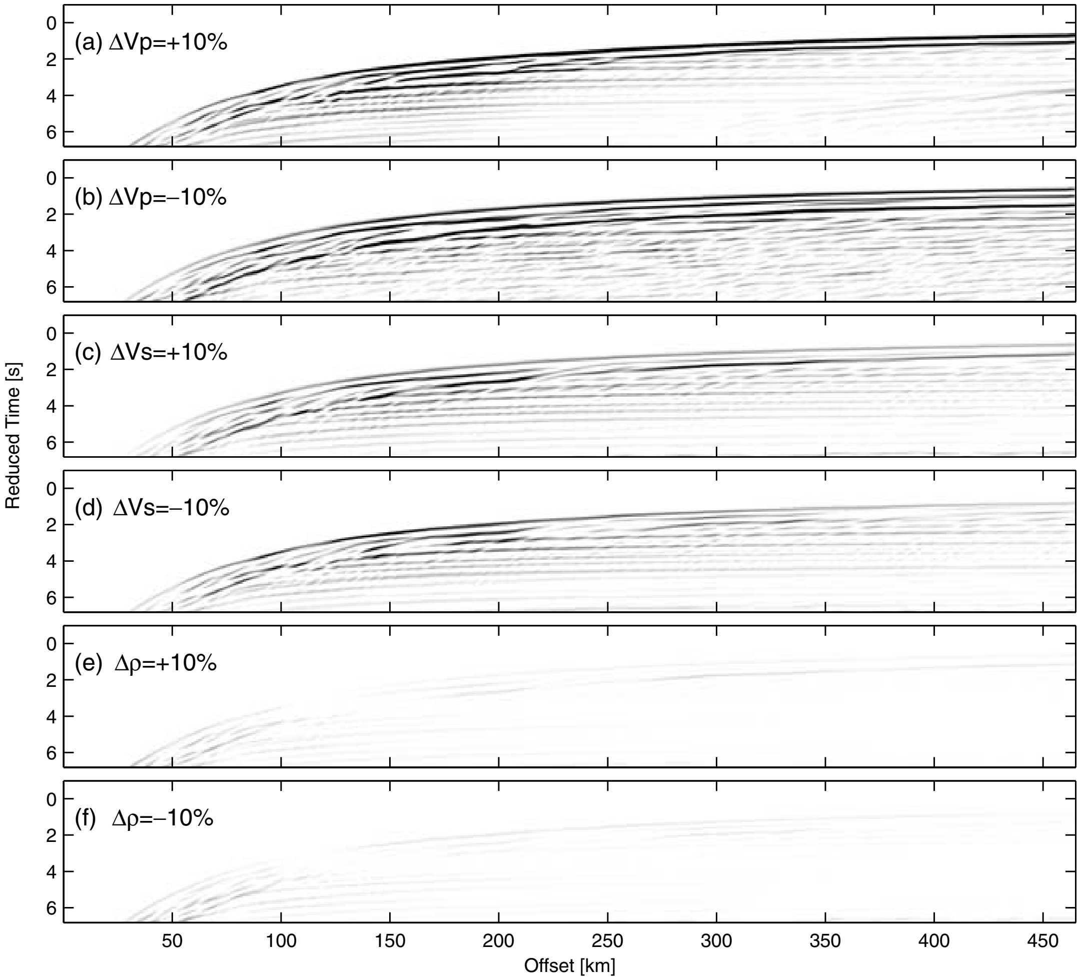

Figure 4. Reflected wide-angle wavefields (at the surface) corresponding to results in Fig. 3, plotted as reduced traveltime versus offset for wavefields propagated 38.2 s. Reduction velocity 8.1 km s^{-1}.

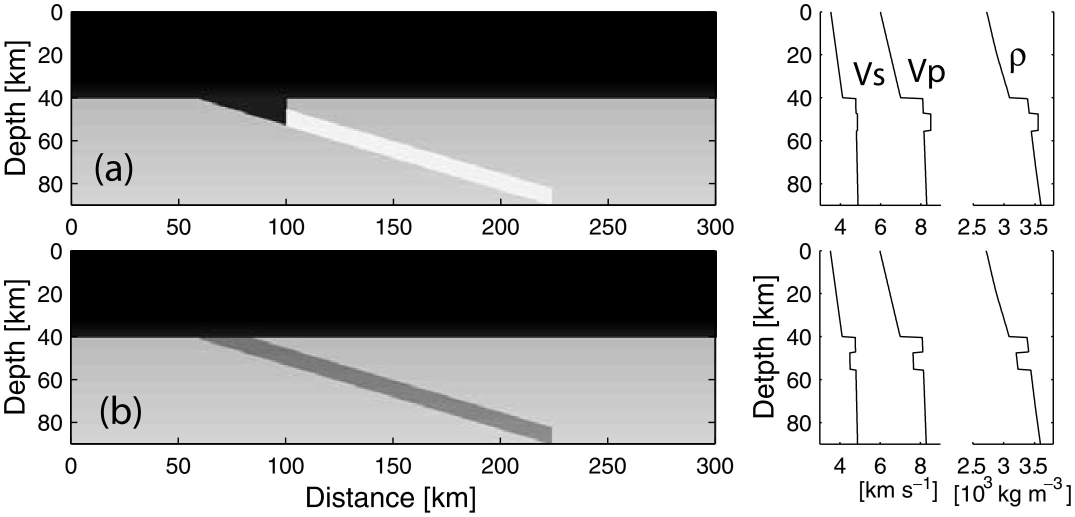

Figure 5. Models of a remnant subduction zone (a) and a shear zone (b). Profiles to the right show velocity and density distribution (at a distance of 110 km). Wavefield modelling is shown in Figs. 6 and 7, with source inserted at distance zero.

affect the seismic wavefield. In the following, the wide-angle seismic wavefield from simplified models of subduction zones and shear zones are investigated. Fig. 5(a) shows a simplified model of a relict subduction and collision model. Balling (2000) suggests two main characteristic features for such regimes: dipping slabs containing eclogite and locally thickened crust with Moho offset, or marked topography on Moho where slabs dip into the upper mantle (see e.g. Fig. 12, later). Fig. 5(b) shows a simple model of an upper-mantle

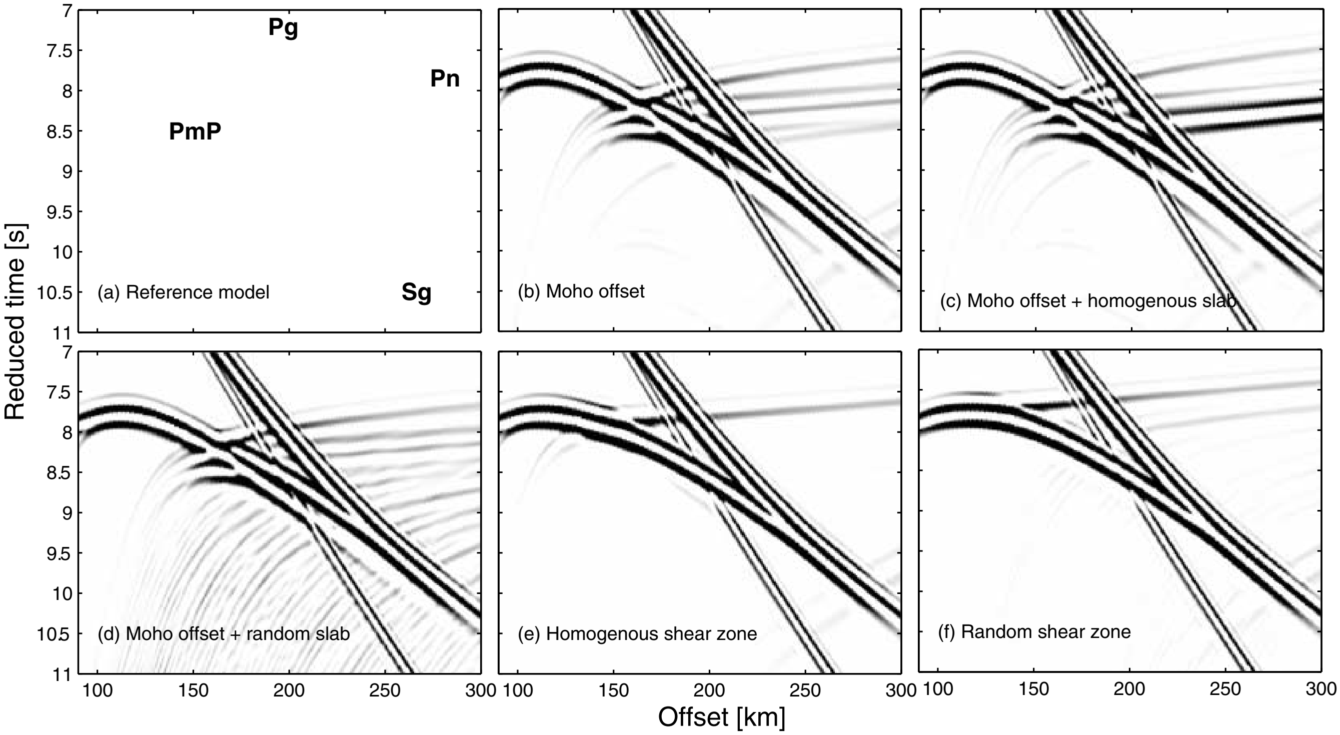

Figure 6. Wide-angle wavefield for models of the type shown in Fig. 5. Reduction velocity 8.0 km s^{-1}. (a) The reference model with a flat Moho and no slab. (b) Moho offset of 12 km at a distance of 100 km, increasing from 60 km. (c) As (b) with a homogeneous high-velocity slab ($Vp = 8.5$ km s^{-1}). (d) As (b) with a slab with a random-velocity distribution: 50 per cent eclogite ($Vp = 8.5$ km s^{-1}) and 50 per cent untransformed crustal material ($Vp = 7.0$ km s^{-1}). (e) Homogeneous low-velocity shear zone (velocity and density reduced by 6 per cent). (f) As (e), however, with a random-velocity distribution in the shear zone consisting of 50 per cent normal mantle material and 50 per cent material with reduced (6 per cent) velocity and density. Same amplification factor for all plots. Difference to reference model is shown in Fig. 7.

dipping shear zone below a flat crust–mantle interface typically observed in extension regimes. These 2-D features are imposed on a simplistic 1-D reference model for the crust and upper mantle. The crust is 40 km thick with a *P*-wave velocity increasing from 6.0 km s^{-1} at the surface to 7.0 km s^{-1} above the Moho. The Vp/Vs ratio is 1.7 and the Vp/ρ ratio is 2.45. The upper mantle consists of our standard reference upper-mantle materials. The computed wavefield from a variety of models based on the two models in Fig. 5 is shown in Fig. 6. The computed wavefield from the 1-D reference model with no Moho offset and no dipping slab in the mantle shows the well known main phases (*Pg*, *PmP*, *Pn* as well as *Sg*, Fig. 6a).

3.4.1 A relict subduction slab

Fig. 6(b) shows the modelled wide-angle field synthetics from a model with locally thickened crust and a Moho offset as the only structure imposed on the reference model. *Pn* can be identified by a series of distinct phases compared to the one distinct *Pn* arrival from the reference model (Fig. 6a). To emphasize the additional phases resulting from introducing sub Moho features, Fig. 7(b) shows the computed wavefield difference to the reference model.

When adding a slab of high-velocity material, a high-amplitude phase following *Pn* can be identified (Figs 6c and 7c). The amplitude of the reflected wave from the slab is of the same magnitude as *Pg* and *PmP*, and a factor of 10 larger than the first arriving *Pn*.

Not all subducted material may transform into eclogite. In particular, if sufficient amounts of fluids are not available, total transformation into eclogite may not occur (e.g. Austrheim *et al.* 1997). Fig. 6(d) shows the computed response from a model with a random distribution of 50 per cent eclogite and 50 per cent untransformed crustal material. *Pn* is followed by an up to 3 s tail of reflected energy. The peak amplitude is smaller than that of a homogenous slab of high-velocity eclogite and at the same level as the first arriving *Pn*. Both high-, medium- and low-velocity eclogite models have been investigated. Only the results from the high-velocity slabs, which produce the greatest wavefield anomalies, are shown, however, significant reflectivity is evident for all types of eclogite when embedded in untransformed crustal material.

3.4.2 A shear zone

If shear zones should be identified in reflection seismic sections, a change in velocity and/or density must occur. A decrease in velocity and density may, as discussed in Sections 2.2 and 3.1.2, result from mylonite reactions, grain diminuition and mechanical mineral changes and orientation as a result of straining. Fig. 6(e) shows the computed wide-angle wavefield from a shear zone (Fig. 5b), where velocity and density are decreased by 0.5 km s^{-1} and 200 kg m^{-3}, respectively, (*ca* 6 per cent) relative to the reference upper-mantle model. The negative reflection coefficient across the boundary to the zone of reduced velocity and density reputedly causes a delay of *Pn*, and the resulting wide-angle wave field shows an apparent *Pn*, arriving approximately 0.4 s later than the *Pn* of the reference model. This will obviously cause some depth errors if one

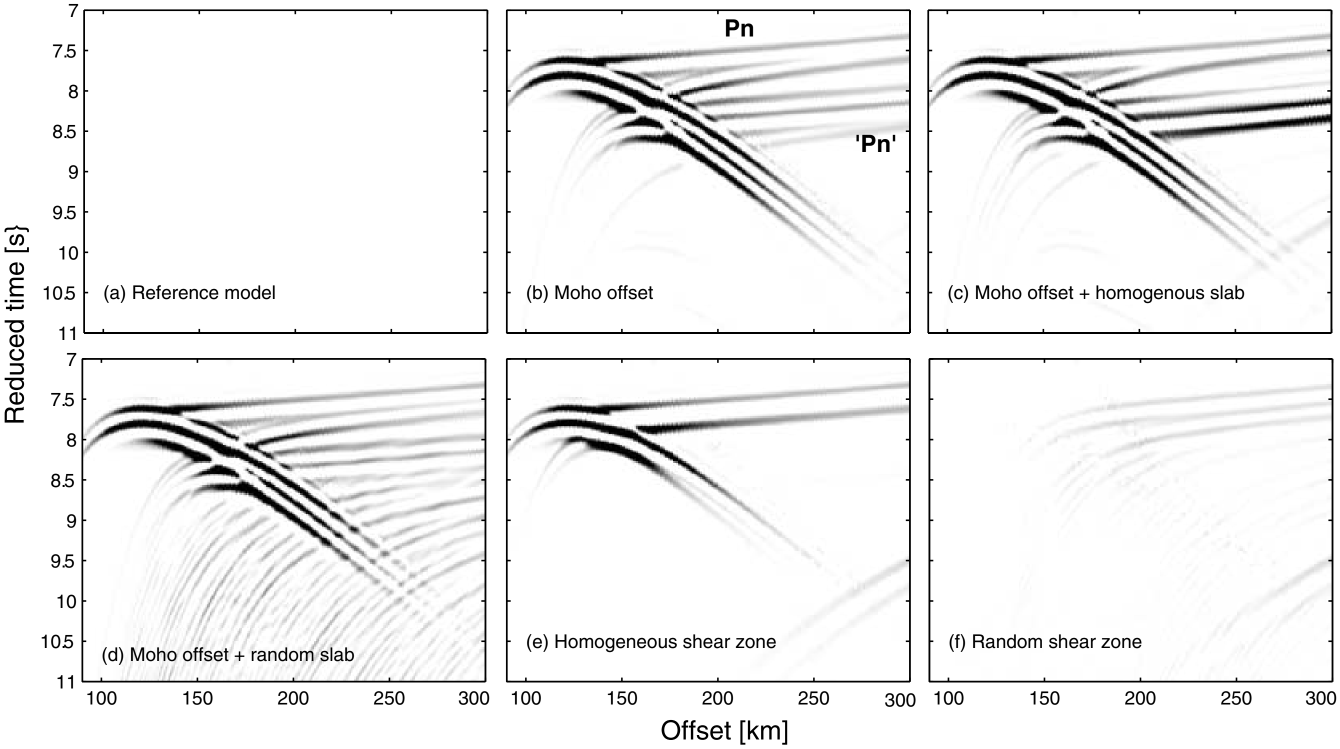

Figure 7. Modelling results as in Fig. 6 showing difference to reference model. Wavefields shown result from introducing the subMoho structural features (Fig. 5). Same amplification factor as in Fig. 6. Note that differences occur as a result of either the generation of new phases or the offsetting arrival times of main phases.

determines a velocity model using the delayed *Pn* as the real *Pn* and without introducing the low-velocity shear zone.

When applying a random distribution of 50 per cent reference material and 50 per cent of the shear model parameters from the previous examples, almost no reflected wavefields can be identified. The computed wavefield is very close to that of the reference model (Figs 6f and 7f). We note that no significant energy is generated from the bottom of the shear zone, neither from the homogeneous nor the stochastic shear zone (Figs 6e , f, 7e and f).

3.4.3 Section summary

For the subduction example, we observe that a Moho offset alone results in a series of complex *Pn* arrivals. The addition of a slab of high-velocity material, embedded in low-velocity untransformed crustal material, causes a strong phase following the *Pn* phase, with amplitudes comparable to those of *PmP* and *Pg*. A slab of partially converted material gives rise to a wide zone of scattered energy following *Pn*, comparable in amplitude to *Pn*.

For the models resembling shear zones, we find that a zone with a drop in velocity and density causes a delay in the apparent *Pn* and only minor modification to the main phases. A zone with randomly-distributed material of reduced velocity and density results in almost no wide-angle seismic energy.

This means that, if a shear zone is represented in the uppermost mantle as a zone of reduced velocity and density, it is unlikely to be recognized in seismic data sets with significant seismic phases in the wide-angle area. On the other hand, if a relict subduction slab is represented in the upper mantle as a zone of partially converted crustal material to high-velocity material, the possibility of observing wide-angle phases clearly exists.

4 OBSERVATIONAL EXAMPLES

4.1 BABEL—southern Baltic sea

In the BABEL project, a marine deep seismic experiment on the Baltic shield and its southwestern margin, with data acquisition in 1989, both near-normal incidence reflection and wide-angle data (using land stations) were recorded, (e.g. BABEL Working Group 1993). Unusually strong energy following the prominent crustal phases and *PmP* can be observed in wide-angle data at station 10, a land station positioned on the island of Bornholm in the southern part of the Baltic sea (Figs 8 and 9). A similar, however, much weaker phase was observed at a nearby station on the Swedish coast (station 11 at Simrisham, BABEL Working Group 1993; Krishna *et al.* 1996). In the same area, dipping near-normal incidence reflectivity is observed beneath the Moho in BABEL line A (Balling 1992, 2000). Reflective structures form 5–10 km long events that can be followed with interruptions for a distance of 75–100 km, from 13 s to 18 s twt (40–65 km depth) with a dip of 15° ENE along the line (Balling 2000).

The recorded wide-angle reflected energy (Rum) is unusual for two reasons: the high amplitude and the relatively short offset at which the phase could be identified (Fig. 9). Nømark *et al.* (1992) used ray tracing to position a dipping reflector in the upper mantle consistent with the Rum arrival times and with the position of dipping features in the reflection seismic data set.

Some efforts have also been made to determine which petrophysical variations may explain the anomalous phase. Krishna *et al.* (1996) modelled the Rum (reflection from upper mantle) phase by introducing a low-velocity zone (7.4 km s^{-1}) in the upper mantle above the reflector and the reflector itself as a structure containing

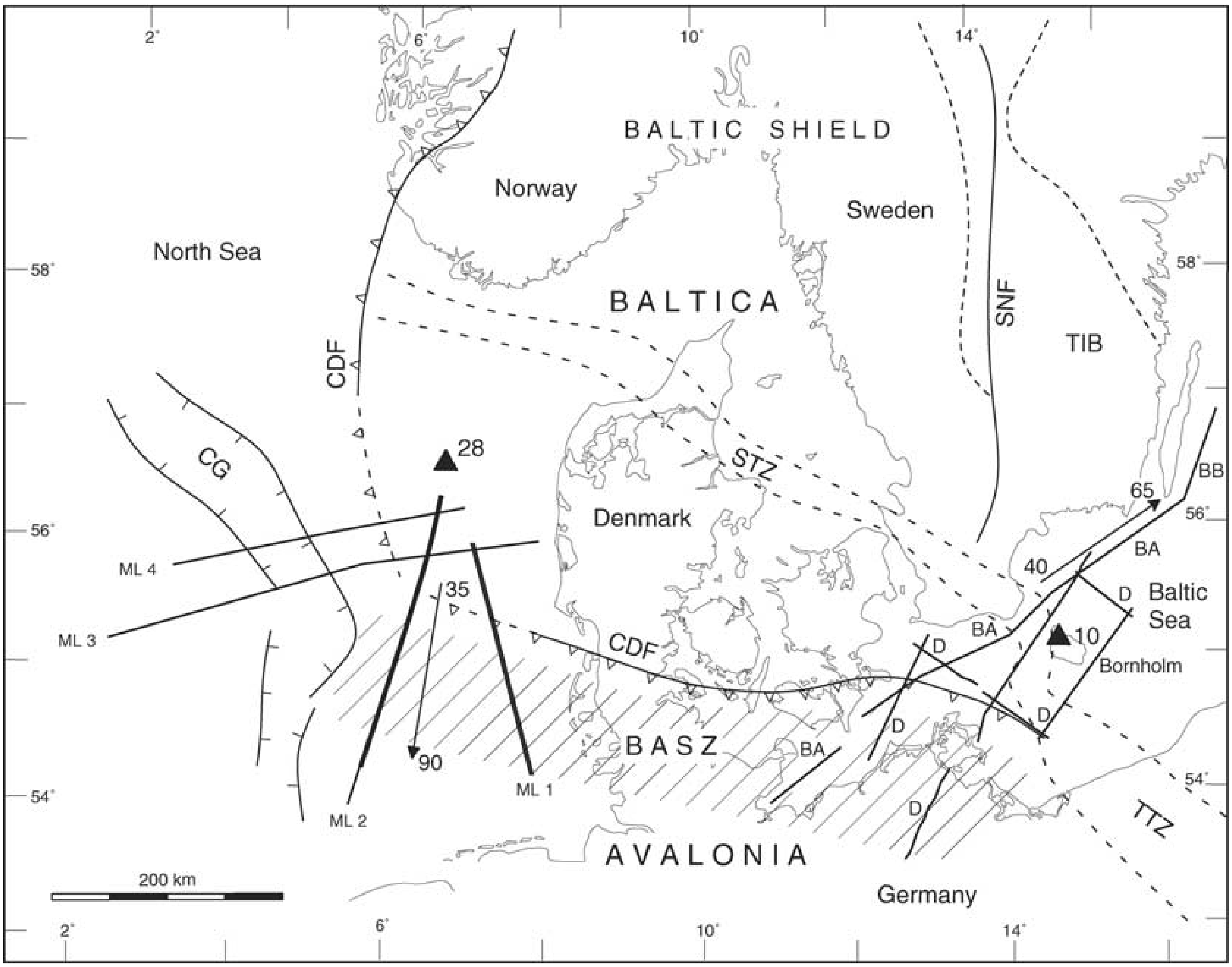

Figure 8. Positions of seismic lines of the MONA LISA (ML 1 to ML 4), BABEL (BA and BB) and DEKORP (D) deep seismic experiments in relation to main structural units of southern Scandinavia, northern Germany and adjacent areas of the North sea and southwestern Baltic sea. This area covers the southwestern part of Baltica, the northeastern part of Avalonia and the Baltica–Avalonia suture zone (BASZ). Further structural units indicated: Caledonian Deformation Front (CDF), Central Graben (CG), Sorgenfrei–Tornquist Zone (STZ), Teisseyre–Tornquist Zone (TTZ), Sveconorwegian Front (SNF), Trans-Scandinavian Igneous Belt (TIB). Solid triangles indicate wide-angle seismic stations (MONA LISA ocean bottom hydrophone station 28 north of ML 2 and BABEL land-station 10 on the island of Bornholm) from which data are analysed in this paper (*cf.* Figs 9 and 13). Arrow along MONA LISA lines 1 and 2 and BABEL line A indicates direction and approximate depth of observed dipping reflectors in the uppermost mantle. Deep near-normal incidence seismic sections from ML 1 and ML 2 (bold sections) are shown in Fig. 12.

two dipping layers each 1 km thick and with velocities of 8.7 and 7.4 km s^{-1}. A large contrast between the low-velocity zone and the high-velocity layer is efficient to produce the relatively high amplitudes.

Balling (2000) argues that the combined observations of dipping normal-incidence reflectivity below the Moho, the wide-angle Rum phase and the geological/tectonic evidence suggest interpretation in terms of a remnant subduction model. The termination of subduction and collisional structural accretion in this area may be approximately 1.77 Ga, the lower age limit for the formation of presumed subduction related Småland-Värmland granitoids within the Trans-Scandinavian Igneous Belt (TIB; Fig. 8), in southern Sweden.

We investigate the seismic response from a model consisting of the ray traced velocity model and position of the source of reflectivity of Rum of Nømark *et al.* (1992) (Fig. 10). Our model includes a 7 km thick dipping layer of elastic properties resembling a remnant subduction slab containing eclogite. The thickness is chosen to simulate former oceanic crust although more complex structures originating from subducted lower continental crustal material are also considered.

Two different models are investigated: a homogeneous (Fig. 10b) and a randomly-distributed (Fig. 10c) velocity field in the dipping slab. The randomly-distributed velocity field is a bimodal von Karman field with fractal dimension 2.75, horizontal and vertical correlation lengths $a_x = a_z = 0.7$ km. A suite of models with different slab velocities has been investigated. Relatively high ($Vp = 8.6$ km s^{-1}), medium ($Vp = 8.3$ km s^{-1}) and lower ($Vp = 7.9$ km s^{-1}) *P*-wave velocities were modelled. For the bimodal field, both velocities typical for uppermost mantle ($Vp = 8.1$ km s^{-1}) and untransformed material ($Vp = 7.0$ km s^{-1}) were considered as background material. Untransformed material refers to either basaltic/gabbroic former oceanic crust or high-grade metamorphic continental lower

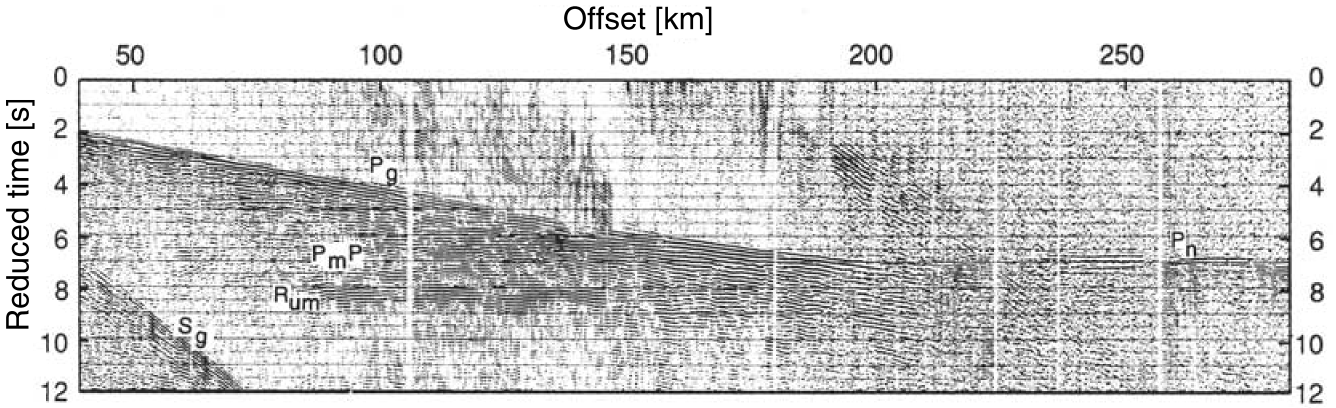

Figure 9. Wide-angle record section from BABEL station 10 (Bornholm). Reduction velocity 8.0 km s^{-1}. A few seconds after the arrival of the high-amplitude *PmP* phase, a strong unusual phase is identified (Rum). It has a remarkably high amplitude at offsets between 85 and 200 km. (After Nømark *et al.* 1992).

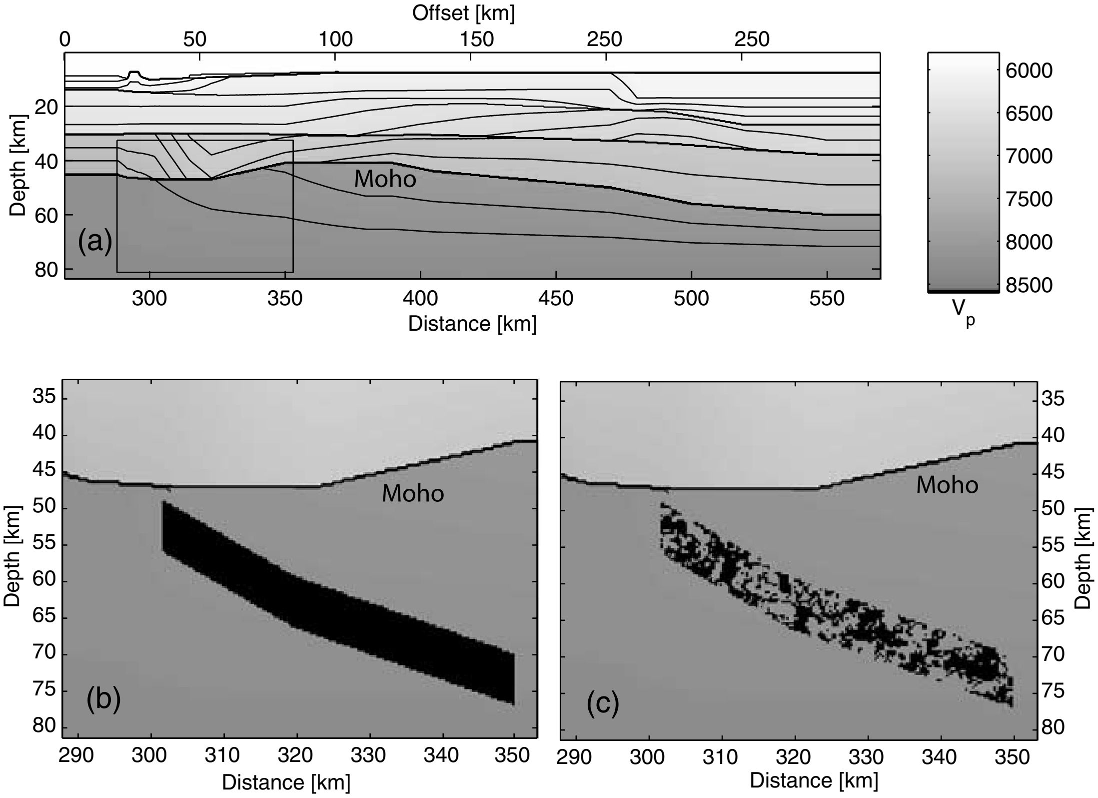

Figure 10. (a) Velocity model from a section of BABEL Line A (BABEL Working Group 1993; Nømark *et al.* 1992). The box denotes the region where a slab is inserted into the model as shown in (b) and (c). (b) Homogeneous slab. (c) Slab with a random-velocity distribution (see text for details). Wavefield modelling results are shown in Fig. 11.

crustal material. The velocity range 7.9 to 8.6 km s^{-1} is meant to include various types of eclogite.

The upper-mantle structure is according to ray tracing models and the near-normal incidence data, dipping about 15°. Considering the recording station position, this will give an incidence angle of about 45°. The Zoeppritz plots of Fig. 2 indicate that an increase in density alone will give no reflectivity at an incidence angle of 45°. When including a significant velocity contrast, reflective energy may become visible.

The computed wavefield from the original ray traced model of Nømark *et al.* (1992) is shown in Fig. 11(a) and the effect of introducing a homogeneous slab of high- and low-velocity material, respectively, is shown in Figs 11(b) and (c). At offsets larger than 150 km (distance along line of about 440 km), both models produce reflected energy of the same amplitude. At smaller offsets, the high-velocity material tends to show more reflected energy. As expected, a slab of intermediate velocity (not shown here) shows almost no reflected energy. Thus both high- and low-velocity material show reflected energy with about the same amplitude with a tendency for larger amplitudes for high-velocity material. However, analyzing the full wavefield plots, it is evident that the amplitudes of the reflected waves from any type of a homogeneous slab of eclogite are

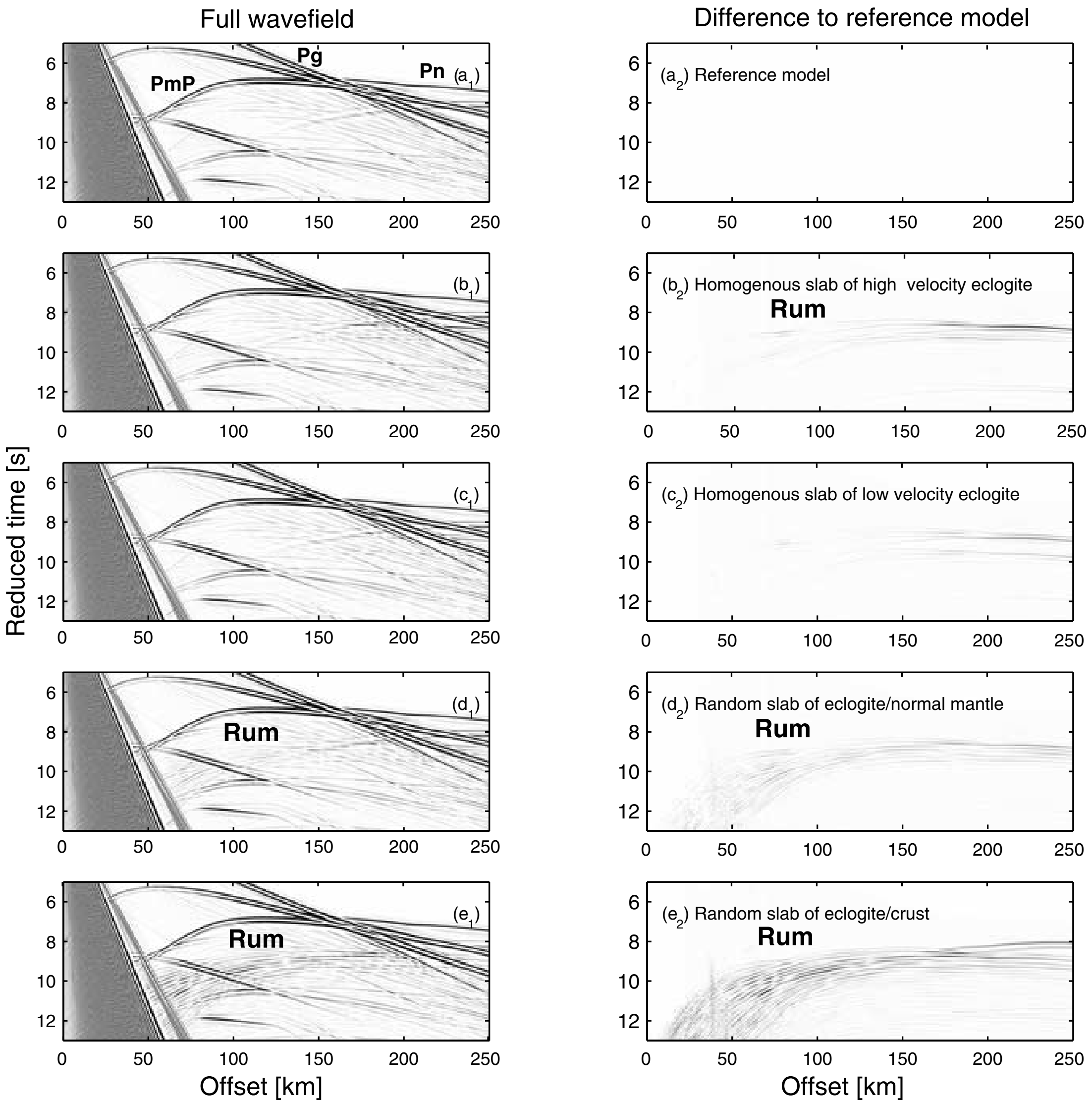

Figure 11. Modelled wide-angle wavefield for models shown in Fig. 10. Reduction velocity 8.0 km s^{-1}. (a) Reference model without dipping slab. (b) Homogeneous slab of high-velocity eclogite ($Vp = 8.6$ km s^{-1}). (c) Homogeneous slab of lower velocity eclogite ($Vp = 7.9$ km s^{-1}). (d) Slab with random-velocity distribution including 50 per cent high-velocity eclogite ($Vp = 8.6$ km s^{-1}) and 50 per cent normal mantle ($Vp = 8.1$ km s^{-1}). (e) Random slab of 50 per cent high-velocity eclogite ($Vp = 8.6$ km s^{-1}) and 50 per cent untransformed crustal material ($Vp = 7.0$ km s^{-1}). The source is positioned at $x = 288.5$ km.

not comparable to those observed for *Pn* and *PmP*. Additionally, no energy is observed at small offsets around 90 km.

Modelling results, using the same structural model as in Fig. 11(b) except with the homogenous velocity distribution replaced by a bimodal velocity distribution of 50 per cent high-velocity eclogite embedded in typical upper-mantle material, are shown in Fig. 11(d). Reflected energy is visible from offsets well below 100 km and out to larger offsets. For offsets below 100 km the seismic wavefield shows noticeable scattered energy. For offsets above about 110 km the reflected energy can be identified as a band of reflected energy very similar to observations (Fig. 9). However, as can be seen, the observed amplitudes of the modelled wavefield are still not sufficiently high to be comparable to those of *Pg*, *Pn* and *PmP*.

In a subducted slab, as noted previously, a full transformation from oceanic or continental crustal material into eclogites does not necessarily happen. Only parts of the slab material may have transformed. This implies a slab including partly crustal-type rock velocities (lower), partly eclogite-type velocities (higher). The modelling results from such semi-transformed slab material, using the same von Karman distribution as in Fig. 11(d), are shown in Fig. 11(e). The modelled amplitudes are now comparable to those of the observed phases. Reflected energy is evident from very short offsets, less than 100 km, and the increased amplitudes result from the significant velocity contrasts within the slab. Modellings (not shown here) show that different kinds of eclogite with high as well as low velocity will produce similar wavefields, thus, resembling the observed wide-angle data recorded at BABEL land-station 10.

The absence of clear wide-angle signals from the Simrisham station and a station on the southern end of the island of Öland (BABEL Working Group 1993; Krishna *et al.* 1996) points towards a rather complex 3-D structure including structural inhomogeneity.

We may conclude that density variations alone within the dipping slab cannot explain the observed Rum phase, and a slab of homogeneous petrophysical properties will neither produce the amplitudes, reflectivity pattern nor explain the short offset at which Rum is observed. However, a random distribution of the velocity field within

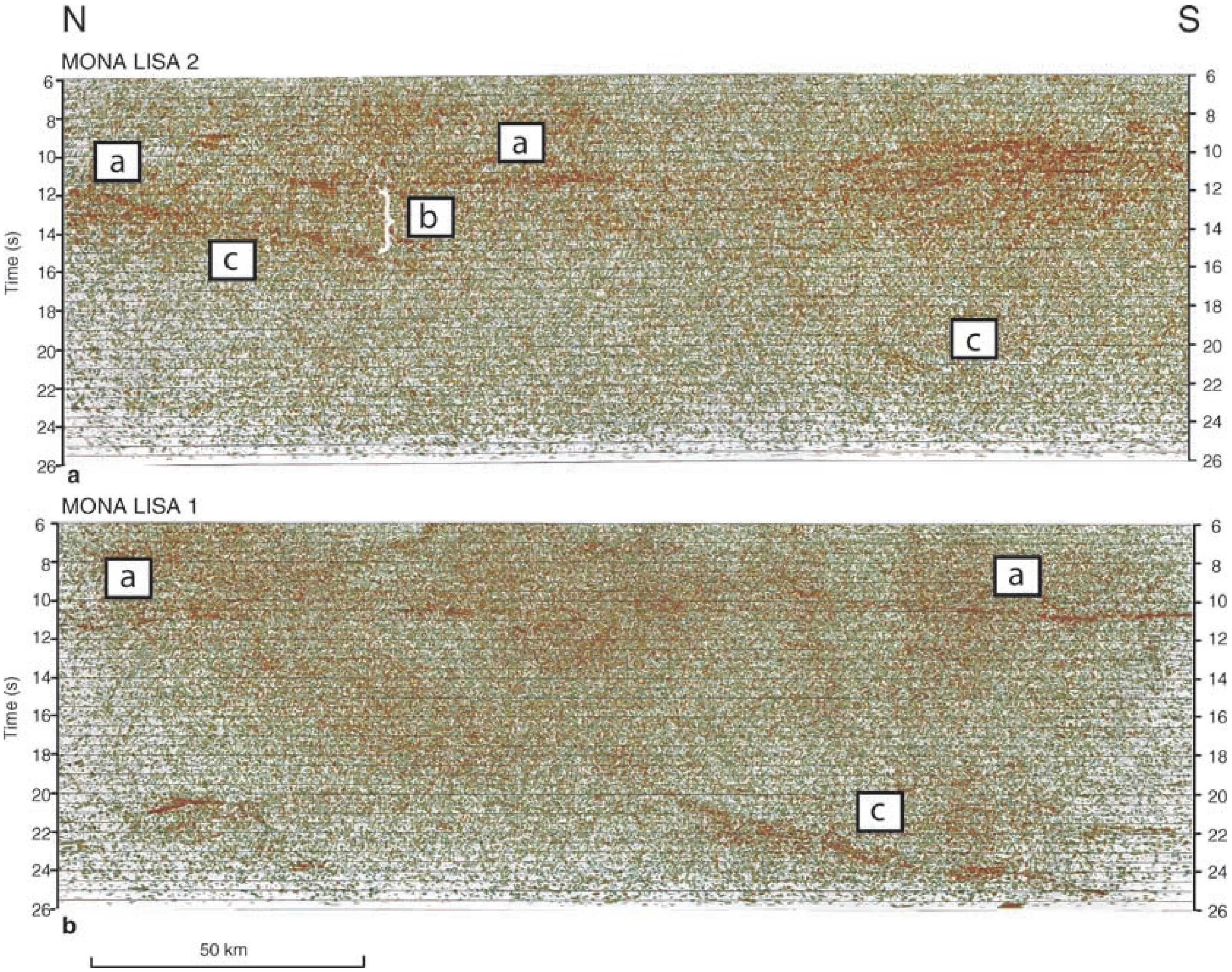

Figure 12. Seismic section for the lower crust and upper mantle (two way traveltimes between 6 and 26 s) along MONA LISA lines 1 and 2 (see Fig. 8): (a) Moho, (b) Moho offset, (c) dipping reflector. (After Balling 2000).

the slab produces the reflectivity pattern and explains the energy observed at small offsets. The internal contrast in elastic parameters must be relatively large to explain the amplitudes. The combination of untransformed former crustal material and various types of eclogite of significantly increased *P*-wave velocity and density, resulting from a partial transformation, most likely will produce such contrasts.

North/northeast dipping mantle reflectors observed southwest of Bornholm in the marine DEKORP deep seismic lines in the area of the Caledonian Deformation Front (Fig. 8) are interpreted to originate from compressive events and not necessarily related to subduction (Krawczyk *et al*. 2002; Meissner *et al.* 2002).

4.2 MONA LISA—southeastern North sea

Seismic near-normal incidence and wide-angle data were recorded in the MONA LISA project to investigate the seismic characteristics of a presumed Caledonian collision between Baltica and Avalonia in the North sea and deep crustal and upper-mantle structures of the Central Graben (MONA LISA Working Group 1997a). Lines 1 and 2 from the survey are striking approximately N–S across the Caledonian Deformation Front (Fig. 8). Near-normal incidence data on both lines 1 and 2 (Fig. 12) show clear southward-dipping reflections in the mantle lithosphere, which can be followed from the crust–mantle boundary to a depth of 80–90 km (MONA LISA Working Group 1997b; Balling 2000). In line 2 a seismic feature indicating a Moho offset zone can be identified (Fig. 12). Also, the wide-angle data set shows indications of seismic energy from below the Moho. In particular, the wide-angle data obtained at station OBH 28, line 2 (Fig. 8), are abnormal compared to the rest of the wide-angle data along that line. The *Pn*, the head wave from below Moho, is highly anomalous and characterized by a band of energy and an apparent high velocity (Fig. 13).

The origin of the seismic energy from the mantle and the tectonic interpretation is a matter of debate. Two models have been proposed: (i) a subduction model with remnant, subducted Tornquist sea oceanic crust dipping to the south below Avalonia (MONA LISA Working Group 1997b; Balling 2000) and (ii) a mantle shear zone associated with the formation of post-collisional (Permian and Mesozoic) sedimentary basins (Abramovitz *et al.* 1998; Abramovitz & Thybo 2000). In previous sections we have argued that there is a great petrophysical difference between such models and a significant difference in the resulting wavefields.

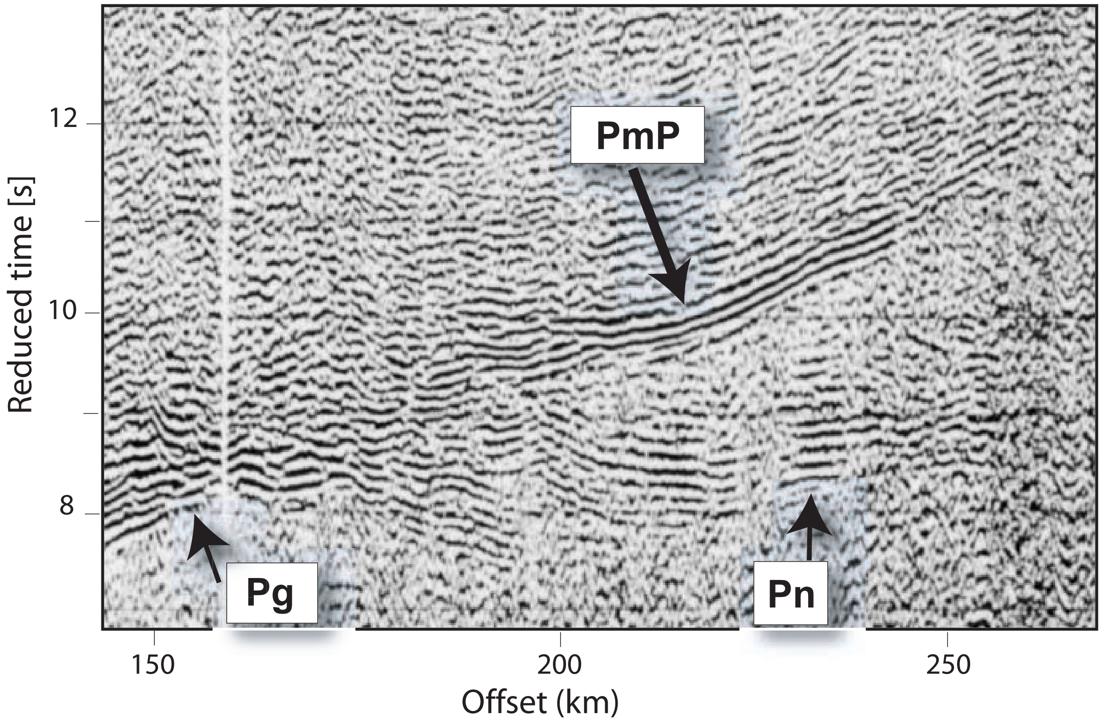

Figure 13. Seismic wide-angle observations from MONA LISA line 2, OBH station 28 (*cf.* Fig. 10). Reduction velocity 8.0 km s^{-1}. (After Abramovitz & Thybo 2000).

Using ray inversion of wide-angle traveltimes from ocean bottom hydrophone data, Abramovitz & Thybo (2000) obtained the velocity model of line 2, shown in Fig. 14(a). This velocity model is generally well constrained as a result of the good ray coverage for the crust and Moho. Additionally, they included a southward-dipping high-velocity structure beneath the Moho (Fig. 14b). This structure includes *P*-wave velocity up to 8.5 km s^{-1}. The dip of the southward-dipping near-normal incidence reflector is 15–20° (Fig. 12).

The velocity model of Abramovitz & Thybo (2000) has a limited number of traveltime picks to constrain velocity and dip of the subMoho slab and does not place the dipping structure at the same depth levels as from where energy is observed in the near-normal incidence data (see fig. 8 in Abramovitz & Thybo 2000). The Moho offset zone clearly indicated in the reflection seismic section of line 2 (Fig. 12) is not included in the above wide-angle velocity models.

Based on the velocity model of Abramovitz & Thybo (2000), the indicated Moho offset zone and southward-dipping near-normal incidence reflectivity, we analyse the remnant subduction and the shear zone interpretational models. In our models, the seismic velocity down to the Moho is identical to that of Abramovitz & Thybo (2000).

As for the BABEL data set, the reflected wavefield for the upper-mantle reflector is investigated using full waveform modelling. For the numerical studies, we use a Gaussian wavelet with peak frequency of 8 Hz, equivalent to observations. A model of 330 km × 80 km and a spatial sampling interval of 50 m result in a model grid of 6600 × 1600 grid cells. 51 s of seismic data were modelled in 15 000 time steps.

The computed wavefield for the model with no upper-mantle slab (Fig. 14a) is similar to many of the wide-angle data sets obtained along line 2. *Pn* is clearly identified as one specific phase (Fig. 15a). Introduction of the high-velocity slab suggested by Abramovitz & Thybo (2000) (Fig. 14b) results in a *Pn* characterized by two main phases (Fig. 15b): the first arriving phase has a higher apparent velocity than the second.

The near-normal incidence section for line 2 (Fig. 12) clearly indicates the existence of a Moho offset zone. A simple Moho offset with thickened lower crust (Fig. 14c) at the position indicated by the near-normal incidence data also results in two *Pn* phases, the first arriving with an apparent velocity slightly larger than the second (Fig. 15c). These *Pn* phases arrive about 0.5 s later than the *Pn* phases modelled in Fig. 15b. If the material within the Moho offset zone is modelled as fully eclogitized material and with a high *P*-wave velocity (8.6 km s^{-1}) (Fig. 14d), only one *Pn* phase, arriving relatively early, can be identified. However, the velocity distribution within the Moho offset zone might result from a mixture of partly eclogitized lower crustal material. Fig. 14(e) shows such a model consisting of a bimodal velocity field with 50 per cent of each material. The wide-angle wavefield is mostly insensitive to such mixtures (Fig. 15e) even though the velocity variation applied for the Moho offset zone is rather large ($Vp_{\text{lower crust}} = 7$ km s^{-1} and $Vp_{\text{eclogite}} =$ 8.6 km s^{-1}). At shorter offsets, below 150 km, scattered energy can be identified. The *Pn*, however, is characterized by a single main arrival.

A slab of dipping homogeneous high-velocity eclogite (8.6 km s^{-1}) attached to a Moho offset zone, positioned along the observed near-normal incidence reflectivity (Fig. 14f), produces a wide-angle wavefield where *Pn* again is characterized by two phases (Fig. 15f). If the dipping slab consists of a mixture of a random distribution of lower crustal material ($Vp = 7$ km s^{-1}) and a high-velocity eclogite (8.6 km s^{-1}; Fig. 14g), the wide-angle wavefield shows a 2 s long ringing *Pn* (Fig. 15g).

The two fast arriving *Pn* phases measured at OBH 28 can be modelled using the velocity model of Abramovitz & Thybo (2000). However, there is inconsistency between the near-normal incidence data

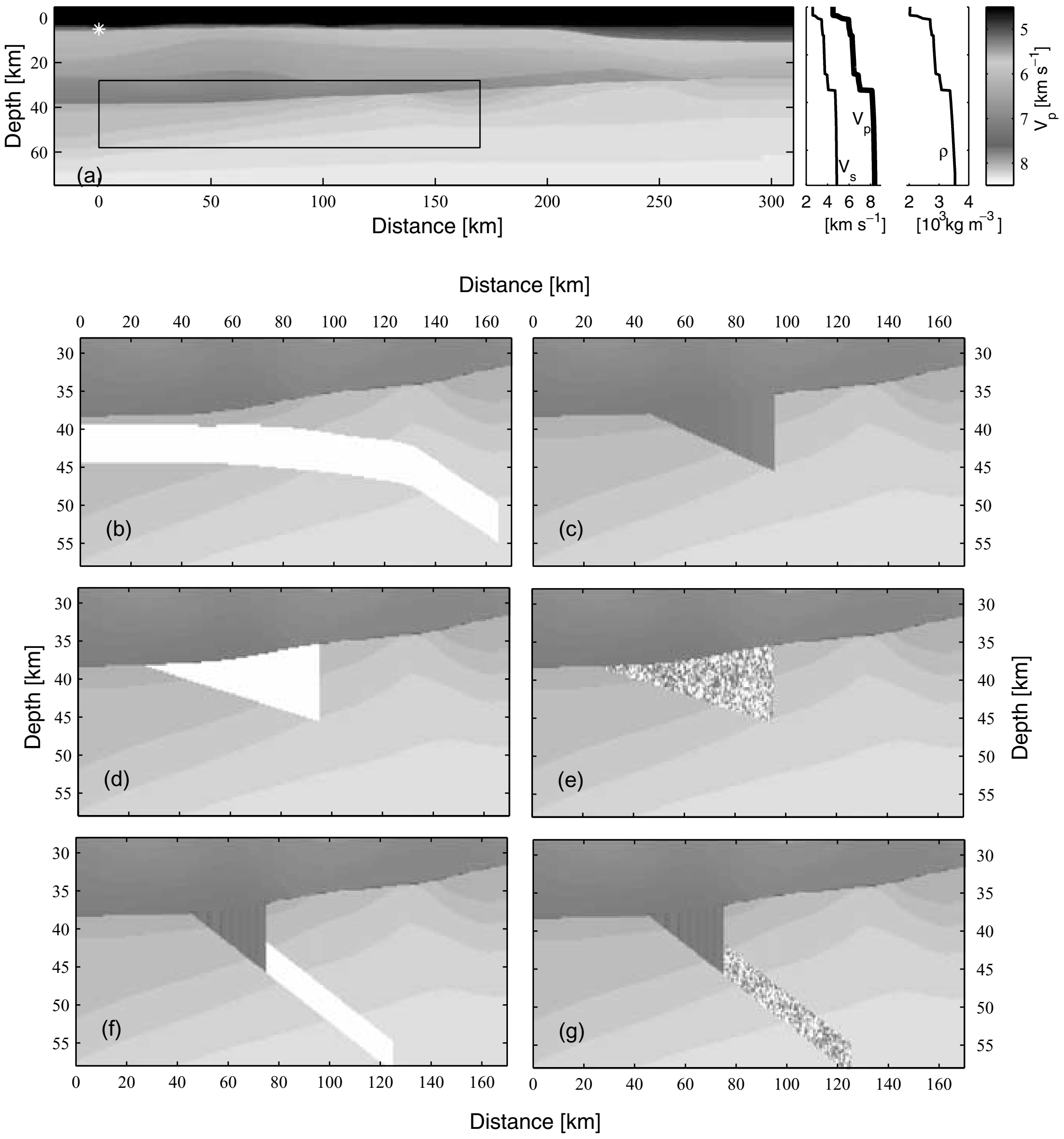

Figure 14. Seismic velocity models for MONA LISA line 2. (a) Velocity model obtained by ray tracing (after Abramovitz & Thybo 2000). Velocity and density profiles to the right are from offset 100 km. Models (b) to (g) include structural features below the Moho. Details of these models are plotted for the region within the framed box. (b) High-velocity slab from Abramovitz & Thybo (2000). (c) Moho offset with thickened crust. (d) Homogeneous high-velocity material (eclogite) in the Moho offset region. (e) A random distribution of a mixture of high-velocity eclogite and untransformed lower crustal material in the Moho offset region. (f) Moho offset with thickened crust and a slab of homogeneous eclogite. (g) Moho offset with thickened crust and a slab with a random distribution of a mixture of high-velocity eclogite and untransformed crustal material. The associated wavefield modellings are shown in Fig. 15.

and the position of the high-velocity slab. Further, the constraints on both the position and the velocity of the slab are guided by few traveltime picks. The models shown in Figs 14(b)–(g) are consistent with the location of observed reflectivity in the near-normal incidence data. A simple Moho offset model is sufficient to produce a double nature *Pn* fairly similar to observations. A double *Pn* phase disappears as complexity is introduced in the Moho offset zone. A dipping slab attached to the Moho offset zone affects the wide-angle wavefield significantly, particularly, if the slab contains a randomly distributed velocity field of relatively high-velocity contrast.

The arrival times of *Pn* modelled in Figs 15(c)–(g) are about 0.5 s later than those observed. This discrepancy may easily be compensated by a minor adjustment in crustal thickness. Thus, our modelling shows that a Moho offset zone, associated with an upper-mantle southward-dipping slab with a random-velocity distribution, produces significant seismic features similar to those observed in the wide-angle wavefield (Fig. 13) and consistent with the near-normal incidence data.

Shear zones like those modelled in Section 3.4.2 (Figs 5b , 6e, f, 7e and f) do not produce wide-angle signals of the type observed. Multiphase *Pn* with relatively high amplitudes is not generated. Shear zones generated in relation to lithospheric extension, crustal thinning and formation of sedimentary basins are unlikely to be associated with local crustal thickening and a Moho offset. The combination of a Moho offset zone and a dipping extensional shear zone, which, from a purely modelling point of view, may produce wide-angle energy similar to that observed, is thus tectonically less realistic. Therefore, our models provide support for the remnant

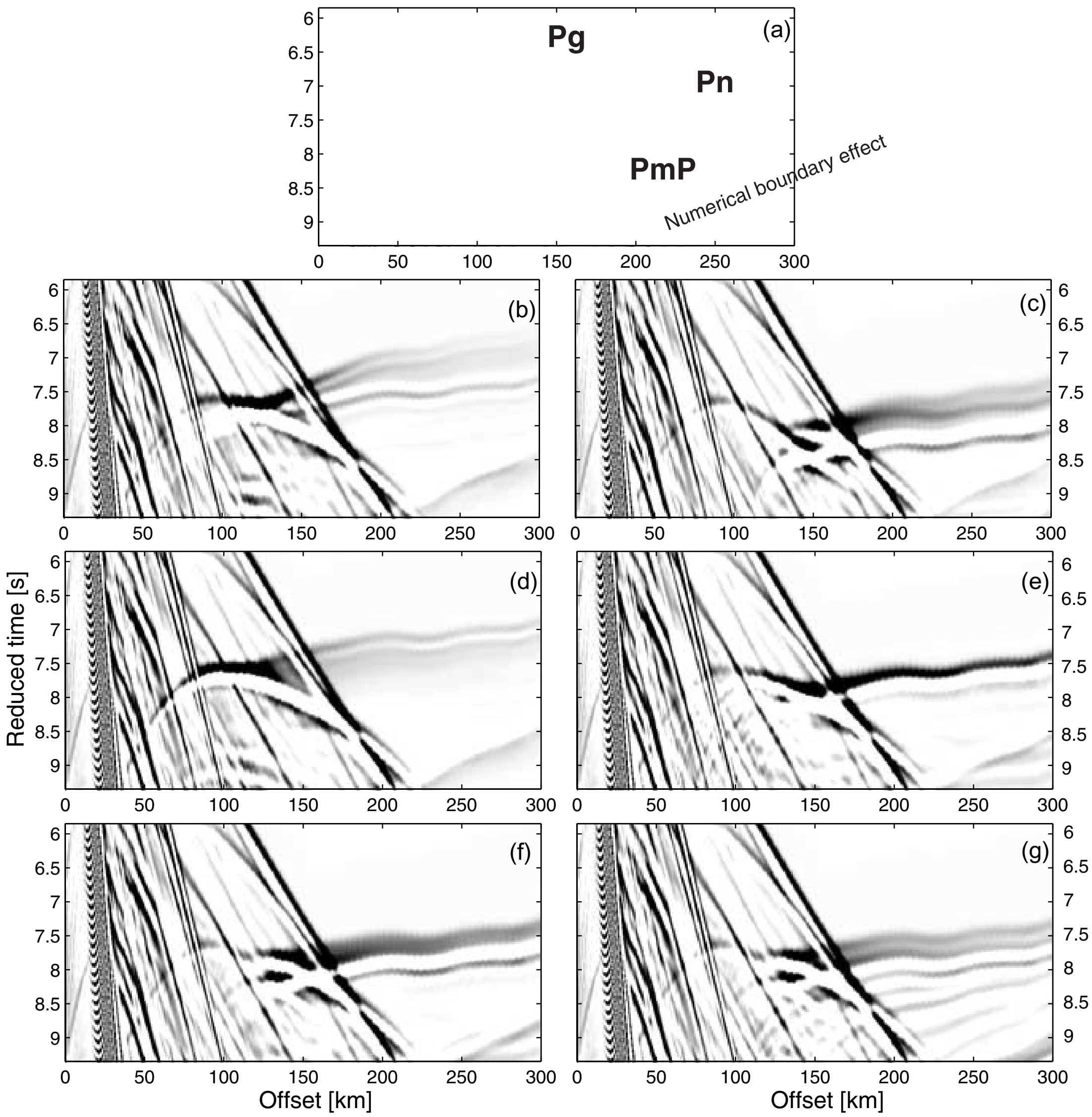

Figure 15. Modelled wide-angle wavefield for models shown in Fig. 14. Reduction velocity 8 km s^{-1}. Results are to be compared to wide-angle observations shown in Fig. 13.

subduction interpretation (Balling 2000) of the southward-dipping upper-mantle reflectivity structures observed in MONA LISA profiles 1 and 2.

The Tornquist sea oceanic crust, which separated Avalonia and Baltica until late Ordovician times (McKerow *et al.* 1991; Torsvik 1998), is suggested to have subducted to the south beneath Avalonia (see also Pharaoh 1999; Banka *et al.* 2002). Remnant subduction features may later, during formation of basins, to some extent have been reactivated in extension, however, without fully flattening the Moho as observed along MONA LISA line 2.

Local northward-dipping reflectors observed just below the Moho in the central part of line 1 and not in line 2 (Fig. 12) are suggested to represent local features, which may be generated either in compression or extension.

5 DISCUSSION

Seismic reflectivity from upper-mantle structures approximated by homogeneous slabs can be studied analytically using the Zoeppritz equations. Valuable general information is obtained and results may be compared to those obtained for inhomogeneous and more complex real-case structures analysed using numerical waveform modelling.

5.1 Homogeneous slab approximation

Using Zoeppritz equations to analyse the amplitude variation with offset, we have seen that a high-velocity eclogite ($Vp \geq 8.2$ km s^{-1}), as expected, will have a positive reflection coefficient at all offsets, however, varying in magnitude. It is relatively large at small and long offsets, and relatively small at intermediate offsets. Intermediate velocity eclogite ($Vp \approx 7.8$ km s^{-1}) will have a positive near-normal incidence reflection coefficient, however, decreasing with offset and changing sign at offsets approximately three times the depth to the reflector. Low-velocity eclogite ($Vp \leq 7.6$ km s^{-1}) shows increasingly negative reflection coefficient with offset. These results show that an eclogite with an intermediate velocity will not show significant reflected wide-angle energy.

Both analytical Zoeppritz modelling and numerical full waveform modelling show that a high- as well as a low-velocity eclogite will produce reflected wide-angle energy of about the same magnitude.

5.2 Randomly-distributed velocity fields

We have shown that distributions of partly eclogitized oceanic or continental crust have significant impact on the wide-angle seismic wavefield. A slab of 50 per cent untransformed crustal material and 50 per cent eclogite embedded in upper mantle shows wide-angle reflectivity comparable in amplitude to that of the prominent crustal phases. This is the case for any *P*-wave velocity of the eclogite. In fact, any type of mixture of relatively low-velocity, low-density crustal material with a high-velocity upper-mantle material may produce significant wide-angle reflected energy. Thus, it is the large internal impedance contrasts that generate the high-amplitude reflections. Subducted oceanic or continental crust partly transformed to high-density, high-velocity eclogite may constitute such rock materials.

5.3 Observed upper-mantle reflectors: shears versus subduction

Two specific deep-seismic data sets, one from the southern Baltic sea (BABEL data) and one from the North sea (MONA LISA data), have been studied with the view of trying to discriminate between two main interpretational models for dipping upper-mantle reflectivity and anomalous wide-angle seismic phases, the remnant subduction and shear zone interpretations. Both data sets include high-quality, coincident, deep-seismic near-normal incidence and wide-angle data.

A shear zone within the upper mantle, modelled with variations in the elastic parameters of ±6 per cent, shows very little reflected energy on wide-angle data: too little to explain observed amplitudes. This is the case both for shear zones with a homogeneous and those with a randomly-distributed velocity field.

The seismic data from BABEL land-station 10 can be explained by a dipping slab of partly eclogitized subducted oceanic or continental crustal material. This both explains the relatively high amplitude and the short offset at which wide-angle energy is observed. The layered model by Krishna *et al.* (1996) also includes materials of significantly different seismic velocities. However, we find their model less plausible on petrological grounds.

From the MONA LISA near-normal incidence data (lines 1 and 2) and local wide-angle data (station 28), consistency is obtained between observations and wavefield modelling results for a crust–mantle model containing locally thickened crust and an associated southward-dipping remnant subduction slab with random, partly eclogitized (oceanic) crustal material. This is different to the model of Abramovitz & Thybo (2000) who argued that the observed seismic phases and their dipping high-velocity slab are likely to be the result of a mantle shear zone.

6 CONCLUSIONS

Our modelling has concentrated on analyzing seismic wavefields and main-phase anomalies associated with anomalous upper-mantle structures. The aim was to improve our understanding of which seismic characteristics may be observed in seismic data reflecting tectonic features in the upper mantle and to improve, on a quantitative basis, our possibilities of distinguishing between different tectonic interpretations. We have focused on two, often competing, alternative tectonic hypotheses for the origin of dipping upper-mantle seismic reflectors: the relict subduction and shear zone models.

The seismically important characteristic of the subduction model is the existence of a dipping slab of former oceanic basaltic crust, fully or partly transformed to eclogites, which show densities above normal upper-mantle and seismic velocities ranging from below to above that of mantle peridotites. Our shear zone models are characterized by a decrease in both density and seismic velocities.

We have found that both upper-mantle shear zones and relict subduction slabs containing eclogites may contain sufficient impedance contrasts to generate near-normal incidence reflectivity. However, both shear zones and homogeneous subduction slabs containing intermediate-velocity eclogites are generally unlikely to contain sufficient contrasts to produce significant wide-angle seismic energy. It is interesting to note that subduction slabs, whether containing high- or low-velocity eclogites, may produce significant seismic energy of approximately equal amplitudes.

In all cases, energy of seismic phases originating from upper-mantle zones of anomalous seismic velocities and densities is significantly increased if homogeneous zones are replaced by zones of inhomogeneous petrophysical properties. The full waveform modelling clearly demonstrates that small-scale inhomogeneities strongly affect the wide-angle seismic wavefield. Approximately maximum petrophysical contrasts may occur within relict subduction slabs containing a mixture of untransformed (oceanic or continental) crustal material of relatively low-density, low-velocity and high-density, high-velocity eclogite. If, for some reason (e.g. lack of sufficiently high temperatures or lack of fluids), a high degree of eclogitization does not occur, such structures may have formed. Also, topography on the crust–mantle boundary, such as major Moho offsets and associated locally thickened lower crust (e.g. in areas where remnant subduction slabs dip into the mantle), significantly affects the wide-angle wavefields. In particular, apparent multiphase *Pn* waves may be generated.

Our analyses of two specific deep-seismic data sets (MONA LISA data from the southeastern North sea and BABEL data from the southern Baltic sea), from which both near-normal incidence and wide-angle seismic energy are observed at traveltimes suggesting anomalous upper-mantle structures, have shown good agreement between observations and modelling results for dipping slabs containing small-scale inhomogeneities, including material of density and seismic velocity significantly above as well as below those of normal upper-mantle values. This observation is met by the relict subduction model including crustal material not fully transformed to eclogite. Our modelling results support a relict subduction interpretation of seismic observation from BABEL line A in the southern Baltic sea and MONA LISA lines 1 and 2 in the southeastern North sea. Other areas of the North sea, such as the Central graben area (also covered by MONA LISA data) also show dipping upper-mantle reflectivity more likely originating from extensional upper-mantle localized shear zones.

In general, our modelling results show that the relict subduction model, as compared with the shear zone model, is more likely to produce both significant near-normal incidence and wide-angle seismic energy. Only if upper-mantle shear zones may be highly inhomogeneous and include materials with a significantly reduced seismic velocity (by *ca* 10 per cent) or be associated with zones of significantly increased velocity and density, which may be the case for present-day active or young fossil subduction zones, may significant wide-angle energy be generated, however, with a significantly lower amplitude than that from a partly eclogitized subduction slab.

Any interpretation of deep seismic data needs proper considerations of available geological, tectonic and petrophysical information. It, also, seems clear that more observational and experimental information on petrophysical characteristics of particularly shear zone mylonites in mantle peridotites is desirable for constraining the range of likely physical parameter variations in seismic models. We find that our modelling results clearly improve our possibilities of distinguishing between two often competing tectonic interpretational models: the relict subduction model and shear zone models.

ACKNOWLEDGMENTS

We thank Bo Holm Jacobsen for his contribution to waveform modelling, discussions and general support throughout this study. Constructive comments after review received from R. Meissner and E. Lüschen are gratefully acknowledged.

REFERENCES

Abramovitz, T. & Thybo, H., 2000. Seismic images of Caledonian, lithosphere-scale collision structures in the southeastern North Sea along MONA LISA profile 2, *Tectonophysics,* **317,** 25–54.

Abramovitz, T., Thybo, H. & MONA LISA Working Group, 1998. Seismic structure across the Caledonian deformation front along MONA LISA profile 1 in the southeastern North Sea, *Tectonophysics,* **288,** 153–176.

Achenbach, J.D., 1973. Wave Propagation in Elastic Solids, North-Holland Publishing Co./American Elsevier, Amsterdam/New York.

Alsdorf, D., Brown, L. & Nelson, D., 1996. Possible upper mantle fabric on seismic profiles from the Tethyan Himalaya and tectonic interpretation, *J. geophys. Res.,* **101,** 25 305–25 320.

ANCORP Working Group, 1999. Seismic reflection image revealing offset of Andean subduction-zone earthquake locations into oceanic mantle, *Nature,* **28,** 341–344.

Anderson, D.L., 1989. Theory of the Earth, Blackwell Science Publications, Oxford.

Austrheim, H., Erambert, M. & Engvik, A.K., 1997. Processing of crust in the root of the Caledonian continental collision zone: the role of eclogitization, *Tectonophysics,* **273,** 129–153.

BABEL Working Group, 1990. Evidence for early Proterozoic plate tectonics from seismic reflection profiles in the Baltic Shield, *Nature,* **348,** 34–38.

BABEL Working Group, 1993. Deep seismic reflection/refraction interpretation of crustal structure along BABEL profiles A and B in the Southern Baltic Sea, *Geophys. J. Int.,* **112,** 325–343.

Balling, N., 1992. BABEL seismic profiles across the southern Baltic Shield and the Tornquist Zone, in *The BABEL Project, First Status Report, Comission of the European Communities*, EUR 14429 EN, 141–146, eds Meissner, R. *et al.*, Commission of the European Communities Directorate-General, Science, Research and Development, Brussels.

Balling, N., 2000. Deep seismic reflection evidence for ancient subduction and collision zones within the continental lithosphere of north-western Europe, *Tectonophysics,* **329,** 259–291.

Banka, D., Pharaoh, T.C. & Williamson, J.P., 2002. Potential field imaging of Palaeozoic orogenic structure in northern and central Europe, *Tectonophysics,* **360,** 23–45.

Calvert, A.J. & Clowes, R.M., 1990. Deep high-amplitude reflections from a major shear zone above the subducting Juan de Fuca plate, *Geology,* **188,** 1091–1094.

Calvert, A.J., Sawer, E.W., Davis, W.J. & Ludden, J., 1995. Archean subduction inferred from seismic images of a mantle suture in the Superior province, *Nature,* **375,** 670–674.

Christensen, N.I. & Mooney, W.D., 1995. Seismic velocity structure and composition of the continental crust: A global view, *J. geophys. Res.,* **100,** 9761–9788.

Christensen, N.I. & Szymanski, D.L., 1988. Origin of reflections from the Brevard Fault Zone, *J. geophys. Res.,* **93,** 1087–1102.

Clowes, R., Brandon, M., Green, A., Yorath, C., Sutherland-Brown, A., Kanasewich, E. & Spencer, C., 1987. LITHOPROBE—southern Vancouver Island: Cenozoic subduction complex imaged by deep seismic reflections, *Can. J. Earth Sci.,* **24,** 31–5.

Cook, F.A., Hall, K.W. & Roberts, B.J., 1998. Tectonic delamination and subcrustal imbrication of the Precambrian lithosphere in the northwestern Canada mapped by LITHOPROBE, *Geology,* **26,** 839–842.

Cook, F.A., Velden, A.J. & Hall, K.W., 1999. Frozen subduction in Canada's northwest territories: LITHOPROBE deep lithospheric reflection profiling of the western Canadian shield, *Tectonics,* **18,** 1–24.

DEKORP-BASIN Research Group, 1999. Deep crustal structure of the Northeast German basin: New DEKORP-BASIN '96 deep-profiling results, *Geology,* **27,** 55–58.

Flack, C.A., Klemperer, S., McGeary, S., Snyder, D. & Warner, M., 1990. Reflections from mantle fault zones around the British Isles, *Geology,* **18,** 528–532.

Fountain, D.M., Hurich, C.A. & Smithson, S.B., 1984. Seismic reflectivity of mylonite zones in the lower continental crust, *Geology,* **12,** 195–198.

Frederiksen, S. & Braun, S.J., 2001. Numerical modelling of strain localization during extension of the continental lithosphere, *Earth planet Sci. Lett.,* **188,** 241–251.

Frederiksen, S., Nielsen, S.B. & Balling, N., 2001. Post-Permian evolution of the Central North Sea: a numerical model, *Tectonophysics,* **343,** 185–203.

Hacker, B.R., 1996. Eclogite formation and the rheology, buoyancy, seismicity and H_2O content of oceanic crust, in *Subduction: Top to Bottom*, Geophys. Monogr. **96,** 337–346, eds Bebout *et al.,*. Un. Monogr, AGU, Washington, DC.

Hansen, T.M. & Jacobsen, B.H., 2002. Efficient finite difference waveform modeling of selected phases using a moving zone, *Computers and Geosciences,* **28,** 819–826.

Hurich, C.H., 1996. Statistical description of seismic reflection wavefields: a step towards quantitative interpretation of deep seismic reflection profiles, *Geophys. J. Int.,* **125,** 719–728.

Jones, T. & Nur, A., 1982. Seismic velocity and anisotropy in mylonites and the reflectivity of deep crustal faults, *Geology,* **10,** 260–263.

Jones, T. & Nur, A., 1984. The nature of reflections from deep crustal fault zones, *J. geophys. Res.,* **89,** 3153–3171.

Klemperer, S.L. & White, N., 1989. Coaxial stretching or lithospheric simple shear in the North Sea ? Evidence from deep seismic profiling and subsidence, in, Extensional Tectonics and Stratigraphy of the North Atlantic Margins, AAPG Memoir, Vol. 46, pp. 511–523, eds Tankard, A.J. & Balkwill, H.R., Tulsa, OK.

Knapp, J. H. *et al.*, 1996. Lithosphere-scale seismic image of the southern Urals from explosion-source seismic reflection profiling, *Science,* **274,** 226–228.

Krawczyk, C.M., Eilts, F., Lassen, A. & Thybo, H., 2002. Seismic evidence of Caledonian deformed crust and uppermost mantle structures in the northern part of the Trans-European Suture Zone, SW Baltic Sea, *Tectonophysics,* **360,** 215–244.

Krishna, V., Meissner, R. & Thomas, S.A., 1996. Unusual sub-Moho events near Bornholm, Baltic Sea: Modelling of BABEL seismic wide-angle data and a tectonic interpretation, *Geophys. J. Int.,* **125,** 193–198.

Levander, A., Hobbs, R.W., Smith, S.K., England, R.W., Snyder, D.B. & Holliger, K., 1994. The crust as a heterogeneous 'optical' medium or 'crocodiles in the mist', *Tectonophysics,* **232,** 281–297.

Lie, J., Pedersen, T. & Husebye, E., 1990. Observations of seismic reflectors in the lower lithosphere beneath the Skagerrak, *Nature,* **345,** 165–168.

McKerow, W.S, Dewey, J.F. & Scotese, C.f., 1991. The Ordovicidan and Silurian development of the Iapetus Ocean, *Paleontol.,* **44,** 165–178(Spec. Paper).

Meissner, R., 1996. Faults and folds, fact and fiction, *Tectonophysics,* **264,** 279–293.

Meissner, R. & Krawczyk, C.H., 1999. Caledonian and Proterozoic terrane accretion in the southwest Baltic Sea, *Tectonophysics,* **314,** 255–267.

Meissner, R., Thybo, H. & Abramovitz, T., 2002. Interwedging and inversion structures around the trans-European suture zone in the Baltic Sea, a manifestation of compressive tectonic phases., *Tectonophysics,* **360,** 265–280.

MONA LISA Working Group, 1997a. Deep seismic investigations of the lithosphere in the southeastern North Sea, *Tectonophysics,* **269,** 1–19.

MONA LISA Working Group, 1997b. Closure of the Tornquist Sea: Constraints from MONA LISA deep seismic reflection data, *Geology,* **51,** 1071–1074.

Morgan, R.P.L., Barton, P.J. Warner, M. Morgan, J. Price, C. & Jones., K., 2000. Lithospheric structure north of Scotland I. *P*-wave modelling, deep reflection profiles and gravity, *Geophys. J. Int.,* **142,** 716–736.

Nielsen, L., Balling, N. & Jacobsen, B.H., 2000. Seismic and gravity modelling of crustal structure in the Central Graben, North Sea. Observations along MONA LISA profile 3, *Tectonophysics,* **328,** 229–244.

Nielsen, L., Thybo, H., Levander, A. & Solodilov, L.N., 2003. Origin of upper-mantle seismic scattering—evidence from Russian peaceful nuclear explosion data, *Geophys. J. Int.,* **154,** 196–204.

Nømark, E., Balling, N. & Nielsen, P.H., 1992. Seismic wide-angle observations from the uppermost mantle in the SW Baltic Sea, in *The BABEL Project, First Status Report, Comission of the European Communities*, EUR 14429 EN, pp. 131–133, eds Meissner, R. *et al.,* Commission of the European Communities Directorate-General, Science, Research and Development, Brussels.

Pharaoh, T.C., 1999. Palaeozoic terranes and their lithospheric boundaries within the Trans-European Suture Zone (TESZ): a review, *Tectonophysics,* **314,** 17–41.

Posgay, K., Hegedus, E. & Timar, Z., 1990. The identification of mantle reflections below Hungary from deep seismic profiling, *Tectonophysics,* **173,** 379–385.

Price, C. & Morgan, J., 2000. Lithospheric structure north of Scotland II. Poisson's ratios and waveform modelling, *Geophys. J. Int.,* **142,** 737–754.

Reston, T., 1990. Mantle shear zones and the evolution of the North Sea basin, *Geology,* **18,** 272–275.

Rudnick, R.L. & Fountain, D.M., 1995. Nature and composition of the continental crust: A lower crustal perspective, *Reviews of Geophysics,* **33,** 267–309.

Shaocheng, J., Long, C., Martignole, J. & Salisbury, M., 1997. Seismic reflectivity of a finely layered, granulite-facies ductile shear zone in the southern Grenville Province (Quebec), *Tectonophysics,* **279,** 113–133.

Sheriff, R.E. & Geldart, L.P., 1995. *Exploration Seismology,* 2nd Edn, Cambridge Univ. Press, Cambridge.

Smythe, D., Dobinson, A., Mcquillin, R., Brewer, J., Matthews, D., Blundell, D.J. & Kelk, B., 1982. Deep structure of the Scottish Caledonides revealed by the MOIST reflection profile, *Nature,* **299,** 338–340.

Sobolev, S.V. & Babeyko, A.Y., 1994. Modeling of mineralogical composition, density and elastic wave velocities in anhydrus magmatic rocks, *Surv. Geophys.,* **15,** 515–544.

Steer, D.N., Knapp, J.H. & Brown, L.D., 1998. Super-deep reflection profiling: exploring the continental mantle lid, *Tectonophysics,* **286,** 111–121.

Tittgemeyer, M., Wenzel, F., & Fuchs, K., 2000. On the nature of Pn, *J. geophys. Res.,* **105,** 16 173–16 180.

Torsvik, T.H., 1998. Paleozoic palaeography: a North Atlantic viewpoint, *Geol. Fören. Stockholm Förhandl.,* **120,** 109–118.

Turcotte, D., 1997. Fractals and Chaos in Geology and Geophysic, 2nd edn, Cambridge University Press, Cambridge, UK.

Vissers, R.L.M., Drury, M.R., Hoogerduijn Strating, E.H. & van der, Wal D., 1991. Shear zones in the upper mantle: A case study in an Alpine lherzolite massif, *Geology,* **19,** 990–993.

Vissers, R.L.M., Drury, M.R., Newman, J. & Fliervoet, T.F., 1997. Mylonitic deformation in upper mantle peridotites of the North Pyrenean Zone (France): implications for strength and strain localization in the lithosphere, *Tectonophysics,* **279,** 303–325.

Vissers, R.L.M., Drury, M.R., Hoogerduijn Strating, E.H., Spiers, C.J. & van der, Wal D., 1995. Mantle shear zones and their effect on lithosphere strength during continental breakup, *Tectonophysics,* **249,** 155–171.

Wang, C.Y., Okaya, D.A., Ruppert, C., Davis, G.A., Guo, T.S., Zhong, Z. & Wenk, H.R., 1989. Seismic reflectivity of the Whipple Mountain shear zone in Southern California, *J. geophys. Res.,* **94,** 2989–3005.

Warner, M.R., Morgan, J.V., Barton, P.J., Morgan, R.P.L., Price, C.E. & Jones, K.A., 1996. Seismic reflections from the mantle represent relict subduction zones within the continental lithosphere, *Geology,* **24,** 39–42.

Warner, M.R. & McGeary, S.E., 1987. Seismic reflection coefficients from mantle fault zones, *Geophys. J. R. astr. Soc.,* **89,** 223–230.

Williamson, P.R. & Worthington, M.H., 1993. Resolution limits in ray tomography due to wave behavior: Numerical experiments, *Geophysics,* **58,** 727–735.